Environment International 133 (2019) 105141

Contents lists available at ScienceDirect

Environment International

journal homepage: www.elsevier.com/locate/envint

Review article

Mn-based catalysts for sulfate radical-based advanced oxidation processes: A review

Jianzhi Huang, Huichun Zhang*

Department of Civil Engineering, Case Western Reserve University, Cleveland, OH 44106, United States

ARTICLE INFO

Handling Editor: Zhen Jason He

Keywords:
Sulfate radical-based advanced oxidation processes
Mn-based catalysts
Peroxymonosulfate
Persulfate
Contaminant oxidation
Crystallinity

ABSTRACT

Sulfate radical-based advanced oxidation processes (AOPs) have drawn increasing attention during the past two decades, and Mn-based materials have been proven to be effective catalysts for activating peroxymonosulfate (PMS) and peroxydisulfate (PDS) to degrade many contaminants. This article presents a comprehensive review of various Mn-based materials to activate PMS and PDS. The activation mechanisms of different Mn-based catalysts (i.e., Mn oxides MnO_x, MnO_x hybrids, and MnO_x-carbonaceous material composites) were first summarized and discussed in detail. Besides the commonly reported free radicals ($SO_4^{-\bullet}$ and $^{\bullet}OH$), non-radical mechanisms such as singlet oxygen and direct electron transfer have also been discovered for selected materials. The effects of pH, inorganic ions, natural organic matter (NOM), dissolved oxygen content, temperature, and the crystallinity of the materials on the catalytic reactivity were also discussed. Then, important instrumentations and technologies employed to characterize Mn-based materials and to understand the reaction mechanisms were concisely summarized. Three common overlooks in the experimental designs for examining the PMS/PDS-MnO_x systems were also discussed. Finally, future research directions were suggested to further improve the technology and to provide a guidance to develop cost-effective Mn-based materials to activate PMS/PDS.

1. Introduction

Over the last a few decades, numerous environmental problems have emerged that require engineering solutions (Agathokleous et al., 2018; Caron-Beaudoin et al., 2019; Dickerson et al., 2019; S. Hou et al., 2019; Liu et al., 2019). Among them, surface water and ground water in many areas are significantly contaminated due to the discharge of a large variety of organic and inorganic contaminants (Afzal et al., 2019; van Veldhoven et al., 2018). For example, bisphenol A (BPA), an endocrine disruptor (Pollack et al., 2018), has been detected in environments such as soil, surface water, and wastewater (Yu et al., 2015). Various technologies have been examined to remove these contaminants, such as adsorption (Y.-Z. Lin et al., 2019; Pan and Zhang, 2012; Tian et al., 2009), membrane separation (Raman et al., 1994), photocatalytic degradation (Houas et al., 2001; Turchi and Ollis, 1990), biological treatment (Atlas, 1981; Béguin and Aubert, 1994), reduction (Chen et al., 2016; Chen and Zhang, 2013; Huang et al., 2019a; Huang et al., 2019c; Jadbabaei et al., 2017), direct oxidation (J. Huang et al., 2018; Taujale et al., 2016; Zhang et al., 2015; Zhou et al., 2019), and advanced oxidation processes (AOPs) (Huang et al., 2019b; Zhang and Lemley, 2006; Zhou et al., 2019). Among these technologies, AOPs are particularly attractive because they are highly reactive and capable of oxidizing a wide range of contaminants, especially those refractory contaminants, to mostly harmless compounds or even complete mineralization to CO_2, H_2O, and inorganic ions (Q. Zhao et al., 2017). In addition, AOPs could be employed as an efficient pretreatment method to degrade toxic organic compounds that might suppress biological treatment processes (Stasinakis, 2008). It should be noted that some AOPs might be costly or form un-desirable byproducts (Nidheesh et al., 2013; Sirés et al., 2014), which limited their practical applications. Numerous efforts have been put to investigate and develop different types of efficient AOPs, for example, various Fenton reactions, ozonation, and sulfate radical-based AOPs, for the removal of these contaminants (Guo et al., 2018; Hao et al., 2016; Ghanbari and Moradi, 2017; Wang and Wang, 2018). In particular, sulfate radical-based AOPs (SR-AOPs) have attracted increasing attention due to their advantages including (1) high redox potential (2.5–3.1 V); (2) working under a wide range of solution pH (Hu and Long, 2016); and (3) a longer life time (30–40 μs vs 20 ns) than hydroxyl radical (Ghanbari and Moradi, 2017; Wang and Wang, 2018).

PMS (HSO_5^-) and PDS ($S_2O_8^{2-}$) are commonly used as the sources for SR-AOPs. Oxone ($2KHSO_5 \bullet KHSO_4 \bullet K_2SO_4$) is usually employed to provide PMS, while sodium persulfate ($Na_2S_2O_8$) and potassium persulfate ($K_2S_2O_8$) are the sources for PDS. It has been reported that the

---

* Corresponding author.
E-mail address: hjz13@case.edu (H. Zhang).

https://doi.org/10.1016/j.envint.2019.105141
Received 20 June 2019; Received in revised form 8 August 2019; Accepted 28 August 2019

distance of the O−O bonds in $KHSO_5$ and $(NH_4)_2S_2O_8$ is 1.460 and 1.497 Å (Anipsitakis and Dionysiou, 2004b) and the bond energy is 140–213.3 and 140 kJ/mol (Ao and Liu, 2017), respectively, indicating that PDS is easier to be cleaved than PMS. However, other studies have suggested that PMS is more easily activated because of its unsymmetrical character (H. Lin et al., 2019). Previous studies have shown that sulfate radicals can be generated through the activation of PMS/PDS by many methods, including heat, metal ions, UV, activated carbon, and metal oxides (Ding et al., 2013; P. Hu et al., 2017; Wang and Wang, 2018).

Various heterogeneous materials including Co-, Ag-, Cu-, and Ru-based catalysts have been reported to effectively activate PMS/PDS to remove contaminants (Hao et al., 2019; Wang and Wang, 2018). Compared with other activation methods such as microwave, thermal, ultrasonic and illumination activation, activation by heterogeneous materials has its own advantages, including requiring less energy, ease of scaling-up, and having high reactivity (Oh and Lim, 2019). However, Co- or Cu-based materials might raise health concerns due to the leaching of toxic metal ions into the aqueous phase, which would inhibit their practical applications; while Ru-based catalysts can be more expensive. In comparison, Mn-based catalysts have a few important advantages, such as low toxicity, high natural abundance, and environmental friendliness (Lu et al., 2012; Taujale et al., 2016); therefore, increasing attention has been paid to the development of Mn-based catalysts for the activation of PMS/PDS. To the best of the authors' knowledge, the first paper that used a Mn-based catalyst (Co_3O_4/MnO_2) in SR-AOP to effectively degrade contaminants (phenol as an example) was reported in 2012 (Liang et al., 2012), which demonstrated that Mn-based catalysts could act as an efficient material for SR-AOPs in water treatment. Since then, many manganese oxides (MnO_x) have been investigated, including those of different phase structures (Huang et al., 2019b; Saputra et al., 2013c; Zhu et al., 2019), Mn oxidation states (Saputra et al., 2013b), and shapes (Saputra et al., 2014a). In addition, a number of new effective Mn-based materials have been synthesized, like octahedral molecular sieve (Luo et al., 2015), α-Mn_2O_3@α-MnO_2-500 (Khan et al., 2018a), Ce/Mn_2O_3 (Tian et al., 2019), and OMS-2/g-C_3N_4 (Li et al., 2017a), as the catalysts for the activation of PMS/PDS. Therefore, it is important to review the progress so far in the activation of PMS/PDS by all known Mn-based materials, which will provide a guidance to synthesize more cost-effective catalysts to remove contaminants of concern from the environment.

In the past several years, there have been a few review papers on the activation of PMS/PDS (Devi et al., 2016; Ghanbari and Moradi, 2017; Hu and Long, 2016; Ike et al., 2018; Liu et al., 2018; Matzek and Carter, 2016; Oh et al., 2016; Oh and Lim, 2019; Wacławek et al., 2017; Wang and Wang, 2018; Xiao et al., 2018; Q. Zhao et al., 2017). For example, different heterogeneous catalysts for SR-AOPs have been reviewed, such as cobalt-based materials (Hu and Long, 2016) and carbon-based materials (Q. Zhao et al., 2017). Various methods to activate PMS/PDS have also been reviewed (Ghanbari and Moradi, 2017; Ike et al., 2018; Sun and Wang, 2015; Wang and Wang, 2018). There are also four review papers that have briefly (in one or two paragraphs) discussed Mn-based materials in the activation of PMS/PDS (Ghanbari and Moradi, 2017; Oh et al., 2016; Sun and Wang, 2015; Xiao et al., 2018). Despite these efforts, no comprehensive review has been published to extensively describe Mn-based catalysts for SR-AOPs. Moreover, novel reaction mechanisms such as the formation of $^1O_2$ and direct electron transfer in SR-AOPs by Mn-based catalysts have not been reviewed. In addition, there is a lack of collection of all instrumentation and technologies that are key to examining Mn-based SR-AOPs. Experimental designs that might affect the observed reactivity and mechanisms also need to be discussed so that future researchers can obtain more accurate reactivity and mechanisms for Mn-based catalysts.

In light of the above information, this review will present a comprehensive summary of all reported Mn-based catalysts in activating PMS/PDS. The synthesis methods of MnO_x were first briefly summarized. The mechanisms of various Mn-based catalysts (MnO_2, MnO_x, MnO_x hybrids, and MnO_x-carbonaceous material composites) were then discussed. After that, different factors affecting the reactivity were reviewed. Then, various important instruments and technologies employed to understand the catalytic reactivity and reaction mechanisms were concisely introduced. Next, three experimental designs were recommended based on the previous published work. Finally, we provided conclusions and future perspectives.

2. Synthesis methods

Mn-based materials exist in many different forms and may contain other elements, which would significantly affect their reactivity. Therefore, it is critical to choose appropriate synthesis methods to obtain the Mn-based materials with desirable physicochemical and structural properties for PMS/PDS activation. A range of synthetic methods have been reported, such as hydrothermal (Saputra et al., 2013c) (Wang et al., 2015a), solvothermal (Saputra et al., 2013a), biosynthesis (Y. Xie et al., 2018), sol-gel (Zhang et al., 2019), hard-template (Y. Huang et al., 2018), and precipitation methods (Pang and Lei, 2016; Tang et al., 2015). The synthesis methods for different MnO_x used to activate PMS/PDS are summarized in Table 1. For example, the hydrothermal method is a typical approach for the synthesis of Mn-based materials such as α-MnO_2 (Wang et al., 2015a), Mn_3O_4-MnO_2 (Z. Zhao et al., 2017), MnO_2/$ZnFe_2O_4$ (Wang et al., 2014b), α-MnO_2@CuO (Luo et al., 2018), and Ce/Mn_2O_3 (Tian et al., 2019). The physicochemical properties of MnO_x could be affected by the reaction conditions including reaction time, temperature, solvent polarity, and the ratio of oxidant/reductant. For instance, increasing the calcination temperature can increase the crystallinity of MnO_2 (Wang et al., 2015b). However, increasing temperature can also change other parameters of MnO_2, like surface area and phase structure. It is reported that δ-MnO_2, δ-MnO_2 and α-MnO_2 were obtained when MnO_x were heated at 60, 100, and 110 °C, respectively, and the surface areas of these three MnO_2 were different (Wang et al., 2015b). Therefore, the changes in surface and structural properties should be considered in order to better understand the reactivity and activation mechanisms of PMS/PDS by Mn-based materials. The details of various synthesis procedures of common Mn-based materials have been reviewed in several previous papers (Brock et al., 1998; Islam et al., 2018), and thus will not be further discussed in this paper.

3. Mechanisms of PMS/PDS activation by MnO_x

Compared with the PMS activation by Mn-based materials (Table 1), there have been only a few papers investigating the activation of PDS by these materials (Table 2). Therefore, this section will focus on PMS with a brief discussion of PDS. All the reported mechanisms in these systems are summarized below.

3.1. Activation of PMS by MnO_x

Manganese dioxides (MnO_2) have been used to activate PMS to remove a number of contaminants, such as phenol, bisphenol A, ibuprofen, and organic dyes (Saputra et al., 2012) (Huang et al., 2019b; C. Liu et al., 2016). It is generally believed that sulfate and hydroxyl radicals were generated during this process, as shown in Eqs. (3.1)–(3.4) (Ghanbari and Moradi, 2017) (H. Lin et al., 2019). Compared with $SO_5^{-\bullet}$, $SO_4^{-\bullet}$ has been regarded as a more important radical in contaminant degradation due to its high reduction potential (Eqs. (3.5) and (3.6)) (Oh et al., 2016). Note that some early papers that used MnO_2 to activate PMS proposed the formation of these two radicals as the major reactants in the system but did not verify their presence (Table 1). Recently, based on the quenching experiments and electron spin resonance (ESR) data, researchers have found that besides radical mechanisms ($SO_4^{-\bullet}$ and $^\bullet OH$), a non-radical mechanism (i.e., $^1O_2$) was also

Table 1
Summary of the reported work on the activation of Oxone (PMS) by Mn-based catalysts.

MnO_x	Synthesis method	Contaminant	Direct oxidation[a]	Reactivity	Mechanism	Stability test	Ref.
Manganese dioxide (MnO_2)							
α-MnO_2	$KMnO_4$:maleic acid = 3:1, then calcination and hydrothermal method	Phenol	NC	[PMS] = 2.0 g/L, [Cat] = 0.4 g/L, 100% removal in 90 mins	Proposed $SO_4^{-\bullet}$ and $^{\bullet}OH$	For MnO_2-300, the reactivity decreased to 70% after the third run, while for MnO_2-140, it is stable.	(Saputra et al., 2012)
α-, β-, and γ-MnO_2	Hydrothermal method	Phenol	NC	[PMS] = 2.0 g/L, [Cat] = 0.4 g/L, 100% removal in 60 mins	Proposed $SO_4^{-\bullet}$ and $^{\bullet}OH$	α-MnO_2 showed similar activity in the third run.	(Saputra et al., 2013c)
β-MnO_2	Hydrothermal method	Phenol	NC	[PMS] = 2.0 g/L, [Cat] = 0.4 g/L, 100% removal in 30 mins; 0.024–0.114 min^{-1}.	Proposed $SO_4^{-\bullet}$ and $^{\bullet}OH$	Decreased from 100% to 60% removal after the third run	(Saputra et al., 2014b)
α-MnO_2	Hydrothermal method	Phenol	NC	[PMS] = 6.5 mM, [Cat] = 0.2 g/L, 100% removal in 30 mins; k: 0.147–0.179 min^{-1}	ESR and quenching test: $SO_4^{-\bullet}$ and $^{\bullet}OH$	Significantly decreased after the fifth run	(Wang et al., 2015a)
α- and δ-MnO_2	Hydrothermal method + calcination	Phenol	NC	[PMS] = 2.0 g/L, [Cat] = 0.2 g/L, k: 0.062–0.32 min^{-1}	ESR and quenching test: $SO_4^{-\bullet}$ and $^{\bullet}OH$	For corolla-like δ-MnO_2, stable	(Wang et al., 2015b)
α-MnO_2	Hydrothermal method	Phenol; 2-chlorophenol; 2,4-dichlorophenol	NC	[PMS] = 0.2 g/L, [Cat] = 0.02 g/L, α-MnO_2 nanowire > α-MnO_2 nanotube k: phenol: 0.017–0.045 min^{-1}; 2-chlorophenol: 0.31–0.075 min^{-1}; 2,4-dichlorophenol: 0.071–0.176 min^{-1}	Proposed $SO_4^{-\bullet}$ and $^{\bullet}OH$	Stable	(Peng et al., 2016)
α-MnO_2	Hydrothermal method	Rhodamine B	NC	[PMS] = 0.2 g/L, [Cat] = 0.1 g/L, 99% removal in 60 min. k: 0.028–0.096 min^{-1}	Quenching test: $SO_4^{-\bullet}$ and $^{\bullet}OH$	Stable	(C. Liu et al., 2016)
δ-MnO_2	Hydrothermal method	Iopamidol	pH 7	[PMS] = 0.1 g/L, [Cat] = 0.2 g/L, k: 0.059 min^{-1}	Quenching test: $SO_4^{-\bullet}$ and $^{\bullet}OH$	Not conducted	(J. Hu et al., 2017)
α-MnO_2	Hydrothermal method	Ciprofloxacin	NC	[PMS] = 1 mM, [Cat] = 0.08 g/L, α-MnO_2 nanoflowers > α-MnO_2 nanorods > α-MnO_2 nanoparticles > commercial MnO_2 k(nanoflowers): 0.045 min^{-1}	Quenching test: $SO_4^{-\bullet}$ and $^{\bullet}OH$	Not conducted	(Deng et al., 2017b)
α-, β-, γ- and δ-MnO_2	α-MnO_2: solid state method; β- and γ-MnO_2: hydrothermal method δ-MnO_2: solvothermal method	BPA	pH 3.07	[PMS] = 1 mM, [Cat] = 0.05 g/L, α- > γ- > β- > δ-MnO_2	ESR and quenching test: $SO_4^{-\bullet}$, $^{\bullet}OH$ and $^1O_2$	not conducted	(Huang et al., 2019b)
Pure manganese oxide (MnO_x)							
Mn_3O_4	Solvothermal method	Phenol	NC	[PMS] = 2.0 g/L, [Cat] = 0.4 g/L, 100% removal in 20 mins	Proposed $SO_4^{-\bullet}$ and $^{\bullet}OH$	Stable	(Saputra et al., 2013a)
MnO,MnO_2, Mn_2O_3,Mn_3O_4	MnO_2: commercially purchased; Mn_2O_3 and Mn_3O_4: calcination of MnO_2; MnO: hydrothermal and calcination	Phenol	NC	[PMS] = 2.0 g/L, [Cat] = 0.4 g/L, Mn_2O_3 > MnO > Mn_3O_4 > MnO_2; $k(Mn_2O_3)$: 0.087–0.154 min^{-1}.	Proposed $SO_4^{-\bullet}$ and $^{\bullet}OH$	Mn_2O_3: 27% for the second run; Heat treatment can enhance its stability.	(Saputra et al., 2013b)
α-Mn_2O_3	Solvothermal and hydrothermal method	Phenol	NC	[PMS] = 2.0 g/L, [Cat] = 0.4 g/L, Mn_2O_3-cubic > Mn_2O_3-octahedral > Mn_2O_3-truncated; $k(Mn_2O_3)$: 0.0042–0.0615 min^{-1}.	Proposed $SO_4^{-\bullet}$ and $^{\bullet}OH$	Mn_2O_3-cubic: stable	(Saputra et al., 2014a)
OMS-2	Reflux method	Organic dyes	NC	[PMS] = 0.25 g/L, [Cat] = 0.25 g/L, 93% removal in 10 min	Quenching test: $SO_4^{-\bullet}$ and $^{\bullet}OH$	Decreased from 93% to 91% removal after the fifth run	(Luo et al., 2015)
Mn_3O_4	Co-precipitation method	Acid red G	pH 7:	[PMS] = 1.0 g/L, [Cat] = 0.5 g/L, 100% removal in 90 min	Quenching test: $SO_4^{-\bullet}$ and $^{\bullet}OH$	Stable	(Tang et al., 2015)
Highly porous, monodisperse manganese oxide	Solvothermal method + calcination	Phenol	NC	[PMS] = 2.0 g/L, [Cat] = 0.2 g/L, Calcination enhanced the reactivity	Proposed $SO_4^{-\bullet}$ and $^{\bullet}OH$	Calcinated at 400 °C had the highest stability	(Q. Liu et al., 2016)

(*continued on next page*)

Table 1 (*continued*)

MnO_x	Synthesis method	Contaminant	Direct oxidation[a]	Reactivity	Mechanism	Stability test	Ref.
α-Mn_2O_3@α-MnO_2	Hydrothermal + calcination	Phenol	NC	[PMS] = 2.0 g/L, [Cat] = 0.4 g/L, *k*: 0.00489–0.124 min^{-1}	ESR: $SO_4^{-\bullet}$ and $^{\bullet}OH$	Calcinated at 350 °*C*, 75% removal for the third run; Calcinated at 400 °*C*, high stability; Calcinated at 550 °*C*, 80% removal for the third run.	(Saputra et al., 2016)
Mn_3O_4-MnO_2	Hydrothermal method	Ciprofloxacin	pH 7	[PMS] = 1.0 mM, [Cat] = 0.1 g/L, *k*: 0.139 min^{-1}	Quenching test: $SO_4^{-\bullet}$ and $^{\bullet}OH$	Stable after the fifth run	(Z. Zhao et al., 2017)
α-Mn_2O_3@α-MnO_2–500	Solvothermal + calcination method	Phenol	NC	[PMS] = 1.0 mM, [Cat] = 0.06 g/L, *k*: 0.05 min^{-1}	ESR and quenching test: $SO_4^{-\bullet}$, $^{\bullet}OH$ and $^1O_2$	90% after the fifth run	(Khan et al., 2018a)
BioMnO_x	Biosynthesis method	Phenol and tetracycline	pH 7	[PMS] = 1.0 g/L, [Cat] = 0.4 g/L, Phenol: 0.106 min^{-1}; tetracycline: 0.0808 min^{-1}	ESR and quenching test: $^1O_2$	Stable	(Tian et al., 2018)
Mn_2O_3@Mn_5O_8	Calcination	Phenol, 4-chlorophenol, 2,4-DP, 2,4,6-trichlorophenol	NC	[PMS] = 1.5 mM, [Cat] = 0.3 g/L, 4-chlorophenol,: 0.06836 min^{-1}	ESR and quenching test: $SO_4^{-\bullet}$, $^{\bullet}OH$, $O_2^{\cdot-}$ and $^1O_2$	Stable	(Khan et al., 2018b)
Amorphous MnO_x (AMO)	Solvothermal	BPA	pH 7	[PMS] = 0.4 mM, [Cat] = 17.4 mg/L, 0.0336 min^{-1}	ESR and quenching test: Non radicals	Not conducted	(Wang et al., 2018)
Fungal manganese oxide	Biosynthesis	BPA	NC	[PMS] = 0.2 g/L, [Cat] = 0.1 g/L, 0.06–0.28 min^{-1}	ESR and quenching test: $SO_4^{-\bullet}$ and $^{\bullet}OH$	Not conducted	(Y. Xie et al., 2018)
OMS-2/γ-MnO_2	Refluxing method	Organic dyes	pH 7.5	[PMS] = 0.2 g/L, [Cat] = 0.2 g/L, 97% removal in 20 min	Quenching test: $SO_4^{-\bullet}$ and $^{\bullet}OH$	Stable	(J. Xie et al., 2018)
MnO_x hybrids							
MnO_2/$ZnFe_2O_4$	Hydrothermal method	Phenol	NC	[PMS] = 2.0 g/L, [Cat] = 0.2 g/L, 0.022–0.032 min^{-1}	ESR and quenching test: $SO_4^{-\bullet}$ and $^{\bullet}OH$	80% removal in 180 min	(Wang et al., 2014b)
$MnFe_2O_4$	Hummers method + solvothermal method	Orange II	NC	[PMS] = 0.5 g/L, [Cat] = 0.05 g/L, 0.012–0.063 min^{-1}	Proposed $SO_4^{-\bullet}$ and $^{\bullet}OH$	Stable	(Yao et al., 2014)
Fe_3O_4-MnO_2	Solvothermal method	4-chlorophenol	NC	[PMS] = 0.5 g/L, [Cat] = 0.2 g/L, 100% removal in 30 min	Quenching test: $SO_4^{-\bullet}$ and $^{\bullet}OH$	Decreased from 100% to 90.78% after the fifth run	(Liu et al., 2015)
OMS-2/Fe_3O_4	Solvothermal method	Acid orange 7	pH 3.75	[PMS] = 0.4 g/L, [Cat] = 0.4 g/L, 97% in 15 min	Quenching test: $SO_4^{-\bullet}$ and $^{\bullet}OH$	Decreased from 94% to 84% after the tenth run	(Wei et al., 2015)
$MnFe_2O_4$	Sol-gel method	DBP	pH 7	[PMS] = 20 μM, [Cat] = 0.1 g/L, 42.3% in 30 min	Quenching test: $SO_4^{-\bullet}$ and $^{\bullet}OH$	2–3% decrease after the seventh run	(Ren et al., 2015)
$MnFe_2O_4$	Hydrothermal + reflux + calcination	Orange II	NC	[PMS] = 2 mM, [Cat] = 0.2 g/L, *k*:0.123 min^{-1}	Quenching test: $SO_4^{-\bullet}$ and $^{\bullet}OH$	87.52% removal after the fifth run	(Deng et al., 2016)
$MnFe_2O_4$	Co-precipitation method	p-Nitrophenol	pH 7	[PMS] = 2 mM, [Cat] = 2 g/L, 97% removal in 2 min	Quenching test: $SO_4^{-\bullet}$ and $^{\bullet}OH$	Stable	(Pang and Lei, 2016)
Fe_3O_4@MnO_2	Hydrothermal method	MB	pH 7.94	[PMS] = 20 mM, [Cat] = 0.3 g/L, 100% removal in 30 min	Quenching test: $SO_4^{-\bullet}$ and $^{\bullet}OH$	> 90% removal after the sixth run	(Zhang et al., 2016)
$Mn_{1.8}Fe_{1.2}O_4$	Solvothermal method	BPA	pH 7.5	[PMS] = 0.2 g/L, [Cat] = 0.1 g/L, *k*:0.1019 min^{-1}	ESR and quenching test: $SO_4^{-\bullet}$ and $^{\bullet}OH$	It can be fully recover after the thermal at 400°C.	(Huang et al., 2017)
Ferromanganese oxide	Sol-gel method	tetracycline	pH 5	[PMS] = 0.4 g/L, [Cat] = 0.4 g/L, 94.3% removal in 30 min	ESR and quenching test: $SO_4^{-\bullet}$ and $^{\bullet}OH$	93% removal after the third run	(Yang et al., 2018)
Mn/Fe_3O_4	Solvothermal method + calcination	BPA	pH 7	[PMS] = 2 mM, [Cat] = 0.2 g/L, When Fe:Mn = 1:1, it achieved the best efficiency; 0.72–1.12 min^{-1} at different temperatures	ESR and quenching test: $SO_4^{-\bullet}$ and $^{\bullet}OH$	Only slightly decrease after the third run	(Du et al., 2018)
FeMn	Hydrotherma l + calcination	BPA, DCP, Rhodamine B	pH 7.5	[PMS] = 0.6 mM, [Cat] = 0.5 g/L, FeMn-350demonstrated better reactivity than FeMn-300 and FeMn-400	ESR and quenching test: $^1O_2$	Not conducted	(Yu et al., 2018)
MnO_2/Fe_3O_4/silica	Thermal decomposition + hydrothermal method	Acid red 73	NC	[PMS] = 2 mM, [Cat] = 0.1 g/L, 98.38% removal in 30 min	Proposed $SO_4^{-\bullet}$ and $^{\bullet}OH$	Not conducted	(Tang et al., 2018)

(*continued on next page*)

Table 1 (*continued*)

MnO_x	Synthesis method	Contaminant	Direct oxidation[a]	Reactivity	Mechanism	Stability test	Ref.
$MnO_2/MnFe_2O_4$	Hydrothermal method	Rhodamine B	NC	[PMS] = 0.4 g/L, [Cat] = 0.2 g/L, 98% removal in 15 min; when the mole ratio of $MnO_2/MnFe_2O_4$ was 7:1, the nanocomposites showed the best reactivity	Proposed $SO_4^{-\bullet}$ and $^{\bullet}OH$	Stable	(Chen et al., 2019)
$Mn_{0.6}Zn_{0.4}Fe_2O_4$	Citrate combustion method	BPA	Partly NC	[PMS] = 0.5 mM, [Cat] = 0.2 g/L, 95.8% removal in 60 min	ESR and quenching test: $SO_4^{-\bullet}$,$^{\bullet}OH$ and $^1O_2$	95.8%, 95%, 90.7% and 84.6% removal for the four runs	(H. Lin et al., 2019)
Co_3O_4/MnO_2	Solvothermal + calcination + impregnation method	Phenol	NC	[PMS] = 0.5 g/L, [Cat] = 0.1 g/L, 0.0165–0.0425 min^{-1}	Proposed $SO_4^{-\bullet}$ and $^{\bullet}OH$	Stable	(Liang et al., 2012)
$Co_xMn_{3-x}O_4$	Hydrothermal + calcination	Rhodamine B	NC	[PMS] = 0.2 g/L, [Cat] = 0.01 g/L, $CoMn_2O_4$: 100% removal in 80 min	Quenching test: $SO_4^{-\bullet}$ and $^{\bullet}OH$	Decreased from 100% to 87% removal after the fifth run	(Yao et al., 2015)
CoMnAl	Hydrothermal method	BPA	pH 3.6	[PMS] = 0.15 g/L, [Cat] = 0.02 g/L, 100% removal in 90 min	Quenching test: $SO_4^{-\bullet}$ and $^{\bullet}OH$	Decreased after the third run; The structure of the catalyst was damaged irreversibly at acid pH, while can be regenerated at neutral pH.	(Li et al., 2015)
$CuO\text{-}Co_3O_4@MnO_2$	Solvothermal + calcination method	Phenol	NC	[PMS] = 0.5 g/L, [Cat] = 0.1 g/L, 100% removal in 100 min	Proposed $SO_4^{-\bullet}$ and $^{\bullet}OH$	84% removal after the third run	(Khan et al., 2017)
$Mn_xCo_{3-x}O_4$	Solvothermal + calcination	Carbamazepine	pH 6	[PMS] = 0.5 mM, [Cat] = 0.05 g/L, 100% removal in 30 min	ESR and quenching test: $SO_4^{-\bullet}$ and $^{\bullet}OH$	Stable	(Deng et al., 2017a)
Co_3MnFeO_6	Sol-gel process	Carbamazepine	pH 5.7, partly NC	[PMS] = 0.4 g/L, [Cat] = 0.2 g/L, 99.2% removal in 30 min; *k*: 0.1749 min^{-1}	ESR and quenching test: $SO_4^{-\bullet}$ and $^{\bullet}OH$	Decreased from 99.2% to 91% removal after the fourth run	(Zhang et al., 2019)
MnO_x/SBA-15	Impregnation + calcination	Butyl paraben	pH 6.5 ± 0.2	NR	ESR and quenching test: $SO_4^{-\bullet}$ and $^{\bullet}OH$	After thermal process, 98.4% removal after the sixth run	(Yang et al., 2016)
MnO_x/silica	Impregnation + calcination	Ibuprofen	NC	[PMS] = 6.25 mM, [Cat] = 1 g/L, 0.0045–0.0377 min^{-1}	ESR and quenching test: $SO_4^{-\bullet}$ and $^{\bullet}OH$	Not conducted	(Yang et al., 2017)
CuO/OMS-2	Refluxing + grinding + calcination	Acid orange 7	pH 7	[PMS] = 0.2 g/L, [Cat] = 0.2 g/L, 96% removal in 15 min	Quenching test: $SO_4^{-\bullet}$ and $^{\bullet}OH$	10% decreased after each run	(Li et al., 2017b)
$CuFe_2O_4$/OMS-2	Solvothermal + calcination + solvent free method	Acid orange 7	NC	[PMS] = 0.65 mM, [Cat] = 0.2 g/L, 95.8% removal in 20 min	Proposed $SO_4^{-\bullet}$ and $^{\bullet}OH$	Slightly decrease after each run	(Ye et al., 2018)
α-MnO_2@CuO	Hydrothermal method + calcination	Organic dye	pH 7.4	[PMS] = 1 mM, [Cat] = 0.1 mM, 99% removal in 0.23 s using dead-end filtration cell	ESR and quenching test: $SO_4^{-\bullet}$ and $^{\bullet}OH$	Not conducted	(Luo et al., 2018)
Mn_3O_4/ZIF-8	Hydrothermal + solvothermal	Rhodamine B	NC	[PMS] = 0.3 g/L, [Cat] = 0.4 g/L, 99.4% removal in 60 min	Quenching test: $SO_4^{-\bullet}$ and $^{\bullet}OH$	96% removal after the fifth run	(L. Hu et al., 2017)
MnO_x–carbonaceous based hybrids							
Mn_3O_4-reduced graphene oxide	Hummer method + solvothermal method	Orange II	pH 7	[PMS] = 1.5 g/L, [Cat] = 0.05 g/L, 100% removal in 2 h	Proposed $SO_4^{-\bullet}$ and $^{\bullet}OH$	Stable	(Yao et al., 2013)
Mn/Fe_3O_4/carbon	Hydrothermal + calcination + solvothermal	Phenol	NC	[PMS] = 2.0 g/L, [Cat] = 0.2 g/L, 100% removal in 120 min	Proposed $SO_4^{-\bullet}$ and $^{\bullet}OH$	Significantly decreased in the third run	(Wang et al., 2014a)
$MnFe_2O_4$-graphene hybrid	Hummers method + solvothermal method	Orange II	NC	[PMS] = 0.5 g/L, [Cat] = 0.05 g/L, 0.012–0.063 min^{-1}	Proposed $SO_4^{-\bullet}$ and $^{\bullet}OH$	Stable	(Yao et al., 2014)
Mn/magnetite/graphene oxide	Hydrothermal method	BPA	pH 7	[PMS] = 0.5 mM, [Cat] = 0.5 g/L, 95% removal in 30 min	ESR and quenching test: $SO_4^{-\bullet}$ and $^{\bullet}OH$	Decreased from 95% to 86% removal in the fifth run	(Du et al., 2016)
OMS-2/g-C_3N_4	Refluxing method	Acid orange 7	pH 7.2	[PMS] = 0.65 mM, [Cat] = 0.2 g/L, 88% removal in 30 min	Quenching test: caged radicals	Stable	(Li et al., 2017a)
OMS-2/carbon nanofiber (OC-2)	Refluxing method	Acid orange 7	pH 7	[PMS] = 0.2 g/L, [Cat] = 0.2 g/L, 98% removal in 20 min	ESR and quenching test: $SO_4^{-\bullet}$ and $^{\bullet}OH$	Stable	(Wang et al., 2019)
Mn/g-C_3N_4	Solvothermal + calcination	Acetaminophen	pH 6.5	[PMS] = 0.8 g/L, [Cat] = 0.05 g/L, 0.1-MnCN < 1-MnCN < 0.25-MnCN < 0.5-MnCN	ESR and quenching test: O_2. - and $^1O_2$	Stable after the fourth run	(Fan et al., 2019)

(*continued on next page*)

Table 1 (*continued*)

MnO_x	Synthesis method	Contaminant	Direct oxidation[a]	Reactivity	Mechanism	Stability test	Ref.
MnO_x/N-doped hollow carbon	Solvothermal method	BPA	NC	[PMS] = 0.2 g/L, [Cat] = 0.06 g/L, 99% removal in 30 min	ESR and quenching test: $SO_4^{-\bullet}$ and $^{\bullet}OH$	Decreased from 99% to 95% removal after the fourth run	(Yu et al., 2019)
γ-MnO_2@$ZnFe_2O_4$/rGO	Hydrothermal method	Phenol	NC	[PMS] = 2 g/L, [Cat] = 0.2 g/L, *k*: 0.094–0.438 min^{-1}	ESR and quenching test: $SO_4^{-\bullet}$ and $^{\bullet}OH$	Stable after the fifth run	(Mady et al., 2019)
Doped MnO_x							
Cu-MnO_2	Hard template method	Phenol	pH 7	[PMS] = 0.4 g/L, [Cat] = 0.3 g/L, 100% removal in 40 min; *k*: 0.073 min^{-1}	ESR and quenching test: $SO_4^{-\bullet}$,$^{\bullet}OH$ and $^1O_2$	Stable	(Y. Huang et al., 2018)
Ce/Mn_2O_3	Hydrothermal method	2,4-Dichlorohenol	pH 7, partly NC	[PMS] = 1 g/L, [Cat] = 0.2 g/L, 100% removal in 90 min; *k*: 0.0668 min^{-1}	ESR and quenching test: $SO_4^{-\bullet}$,$^{\bullet}OH$ and $^1O_2$	Stable after the fifth run	(Tian et al., 2019)
Co-biogenic MnO_x	Biosynthesis + impregnation calcination method	Tetracycline	NC	[PMS] = 0.2 g/L, [Cat] = 0.2 g/L, 100% removal in 25 min	ESR: $SO_4^{-\bullet}$ and $^{\bullet}OH$	Slightly decreased after the fifth run	(Luo et al., 2019)
Other Mn-based materials							
$LaMnO_3$	Sol-gel method	Ofloxacin and phenol	NC	[PMS] = 0.5 g/L, [Cat] = 0.2 g/L, *k*: 0.088 min^{-1} for ofloxacin and 0.042 min^{-1} for phenol	ESR and quenching test: $^1O_2$ dominant	Not conducted	(Tian et al., 2017)
$LaMnO_3$	Sol-gel method	Ofloxacin	NC	[PMS] = 0.5 g/L, [Cat] = 0.2 g/L, *k*: 0.0803 min^{-1}	ESR and quenching test: $^1O_2$ dominant	Stable	(P. Gao et al., 2019)
$La_{0.4}Sr_{0.6}MnO_{3-\delta}$	Sol-gel method	Phenol	NC	[PMS] = 2 g/L, [Cat] = 0.2 g/L, *k*: 0.0608 min^{-1}	ESR and quenching test: $^1O_2$ dominant	Stable	(Miao et al., 2019)
$LaCo_{1-x}Mn_xO_{3+\delta}$	Sol-gel method	Phenol	NC	[PMS] = 6.5 mM, [Cat] = 0.1 g/L, *k*: 0.006–0.089 min^{-1}	ESR and quenching test: $SO_4^{-\bullet}$ and $^{\bullet}OH$	Heat treatment can recover the reactivity	(Miao et al., 2018)
Co-Mn LDH	Coprecipitation	Acid orange G	NC	[PMS] = 0.1 g/L, [Cat] = 0.025 g/L, 100% removal in 4 min	Quenching test: $SO_4^{-\bullet}$ and $^{\bullet}OH$	Stable	(Zhao et al., 2018)
Mn-Fe LDH	Coprecipitation	Acid orange 7	NC	[PMS] = 0.2 g/L, [Cat] = 0.2 g/L, 97.56% removal in 30 min	ESR and quenching test: $SO_4^{-\bullet}$ and $^{\bullet}OH$	Stable	(L. Hou et al., 2019)

[a] NC means "direct oxidation not considered at acidic conditions"; "Cat" means "catalysts".

Table 2
Summary of the reported work on the activation of peroxydisulfate (PDS) by Mn-based catalysts.

MnO_x	Synthesis	Contaminants	Reactivity	Mechanism	Stability test	Ref.
Manganese dioxides (MnO_2)						
δ-MnO_2	Hydrothermal method with dropwise addition	Nitrobenzene	*k*: 0.0048–0.0054 d^{-1}	[PDS] = 0.5 M, [Cat] = 1 g/5 mL, Proposed reactive oxygen species without further evidence	Not conducted	(Ahmad et al., 2010)
α-MnO_2	Hydrothermal method	2,4-Dichlorophenol	90.2% removal in 180 min	[PDS] = 20 mM, [Cat] = 0.2 g/L, Scavenger test and ESR: $SO_4^{-\cdot}$ and $^{\cdot}OH$	Decreased from 93% to 81.2% in 360 min after the fifth run	(Zhao et al., 2016)
MnO_2	Hydrothermal method	Acid orange 7	98.1% removal in 30 min	[PDS] = 4.2 mM, [Cat] = 0.6 g/L, Scavenger test: $SO_4^{-\cdot}$ and $^{\cdot}OH$, $HO_2^{\cdot-}/O_2^{\cdot-}$	98.1%, 91.8%, 91.8%,91.8% for the four run	(Xu et al., 2017)
α-, β-,and γ-MnO_2	Hydrothermal method	Phenol	α: 0.0441 min^{-1}; β: 0.0264 min^{-1}; γ: 0.0018 min^{-1}	[PDS] = 4 mM, [Cat] = 0.4 g/L, β-MnO_2: Scavenger and ESR: $^1O_2$	Not conducted	(Zhu et al., 2019)
Pure MnO_x						
MnO	Solvothermal method	CCl_4	0.014–0.026 h^{-1}	[PDS] = 1 g/L, [Cat] = 0.25 g/L, Proposed mechanism: $O_2^{\cdot-}$	Not conducted	(Do et al., 2013)
α-Mn_2O_3, Mn_3O_4, γ-MnOOH	α-MnO_2: solvothermal method; Mn_3O_4, γ-MnOOH: calcination	Phenol	γ-MnOOH demonstrated better reactivity than α-MnO_2 and Mn_3O_4	[PDS] = 2 g/L, [Cat] = 1 g/L, Scavenger test and ESR: $SO_4^{-\cdot}$ and $^{\cdot}OH$	Slightly decreased under neutral and alkaline conditions	(Li et al., 2016)
Nanozerovalent Mn	Chemical reduction method	Ciprofloxacin	95% removal in 80 min	[PDS] = 0.05 g/L, [Cat] = 1 g/L, Scavenger test: $SO_4^{-\cdot}$ and $^{\cdot}OH$	Not conducted	(Shah et al., 2019)
MnO_x hybrids						
Fe_2O_3-MnO	Solvothermal method	CCl_4	0.024–0.043 h^{-1}	[PDS] = 1 g/L, [Cat] = 0.25 g/L, Proposed mechanism: $O_2^{\cdot-}$	Not conducted	(Do et al., 2013)
CaO-Fe_2O_3-MnO	Solvothermal method	CCl_4	0.01–0.04 h^{-1}	[PDS] = 1 g/L, [Cat] = 0.25 g/L, Proposed mechanism: $O_2^{\cdot-}$	Not conducted	(Do et al., 2013)
Iron oxide/MnO_2	Solvothermal method	CCl_4, benzene	CT:0.023–0.048 h^{-1}; Benzene: 0.052–0.074 h^{-1}	[PDS] = 1 g/L, [Cat] = 0.25 g/L, Scavenger test: both oxidants ($SO_4^{-\cdot}$ and $^{\cdot}OH$) and reductants ($O_2^{\cdot-}$)	Not conducted	(Jo et al., 2014a)
Mn-Ca-FeOOH	Solvothermal method	Methylene blue	62% removal in 5 min	[PDS] = 2.5 mM, [Cat] = 1 g/L, Proposed mechanism: $SO_4^{-\cdot}$, $^{\cdot}OH$ and $O_2^{\cdot-}$	Not conducted	(Jo et al., 2014b)
$MnFe_2O_4$-bentonite	Co-precipitation method	2,4-dichlorophenol	92% removal in 240 min	[PDS] = 10 mM, [Cat] = 5 g/L, Scavenger test and ESR: $SO_4^{-\cdot}$ and $^{\cdot}OH$	Decreased from 92% 87% removal after the fifth run	(Y. Zhao et al., 2017)
Fe_3O_4-α-MnO_2	Hydrothermal method	BPA	92% removal in 90 min; *k*: 0.0196 min^{-1}	[PDS] = 30 mM, [Cat] = 1.2 g/L, Scavenger test: $SO_4^{-\cdot}$ and $^{\cdot}OH$	Not conducted	(Dong et al., 2019)
γ-Fe_2O_3/Mn_3O_4	Hydrothermal method	Rhodamine B	γ-Fe_2O_3/Mn_3O_4 (3:1) showed the highest reactivity, with 95.6% removal in 150 min	[PDS] = 50 mg/L, [Cat] = 50 mg/L, Proposed mechanism: $SO_4^{-\cdot}$ and $^{\cdot}OH$	Not conducted	(Ma et al., 2019b)
CuO/$MnFe_2O_4$	Coprecipitation + impregnation method	levofloxacin	87% removal in 120 min	[PDS] = 1 g/L, [Cat] = 1 g/L, Scavenger test: $SO_4^{-\cdot}$ and $^{\cdot}OH$	13.9% decrease after the fourth run	(Ma et al., 2019a)

operative when using different phase structures of MnO_2 to activate PMS, as shown in Eq. (3.7) (Huang et al., 2019b). It has also been demonstrated that $SO_4^{-\bullet}$, $^{\bullet}OH$ and $^1O_2$ were not involved in BPA degradation in PMS-amorphous MnO_x (Wang et al., 2018). The authors proposed that the formed reactive complex between PMS and the MnO_x might have mediated direct electron transfer between BPA and PMS, resulting in the BPA degradation.

$$HSO_5^- + 2MnO_2 \rightarrow SO_5^{-\bullet} + OH^- + Mn_2O_3 \tag{3.1}$$

$$HSO_5^- + Mn_2O_3 \rightarrow SO_4^{-\bullet} + H^+ + 2MnO_2 \tag{3.2}$$

$$SO_4^{-\bullet} + H_2O \rightarrow HO^{\bullet} + H^+ + SO_4^{2-} \tag{3.3}$$

$$SO_4^{-\bullet} + OH^- \rightarrow HO^{\bullet} + SO_4^{2-} \tag{3.4}$$

$$SO_5^{-\bullet} + e^- \rightarrow SO_5^{2-} \qquad E^0 = 1.10 \tag{3.5}$$

$$SO_4^{-\bullet} + e^- \rightarrow SO_4^{2-} \qquad E^0 = 2.60 \tag{3.6}$$

$$2HO^{\cdot} \rightarrow {}^{1}\!/_{2}\,{}^{1}O_2 + H_2O \tag{3.7}$$

For MnO_2, different properties have been reported to affect the reactivity. It has been shown that α-MnO_2 was more reactive than β- and γ-MnO_2 (Saputra et al., 2013c), and the authors suggested a few possible reasons for this, such as tunnel sizes, oxygen liability, and MnO_6 edges. Huang et al., 2019b obtained similar results: α-MnO_2 > γ-MnO_2 > β-MnO_2 > δ-MnO_2, and the authors established linear relationships between some of the physiochemical properties and the catalytic reactivity for the crystalline MnO_2. The results showed that the catalytic reactivity was linearly correlated with the Mn(III) content, Mn average oxidation state (AOS), and conductivity. Moreover, α-MnO_2 with different shapes exhibited different catalytic reactivity on the activation of PMS, with α-MnO_2 (nanowire) > α-MnO_2 (nanorod) > α-MnO_2 (nanotube), which was ascribed to their different surface areas and the activity of different facets of MnO_2 (Wang et al., 2015a).

Besides MnO_2, other MnO_x such as MnO, Mn_2O_3, Mn_3O_4, and OMS-2 have also been used to activate PMS (Saputra et al., 2013b, 2014a). The catalytic reactivity of MnO_x on the activation of PMS was dependent on the Mn oxidation state, with the trend: Mn_2O_3 > MnO > Mn_3O_4 > MnO_2 (Saputra et al., 2013b). Mn_2O_3 with different shapes also had different reactivity, with the order Mn_2O_3 (cubic) > Mn_2O_3 (octahedra) > Mn_2O_3 (truncated) (Saputra et al., 2014a). Similar to MnO_2, sulfate and hydroxyl radicals were also considered to be the major reactive species when PMS was activated by these MnO_x (Eqs. (3.8) and (3.9)).

$$HSO_5^- + 2MnO \rightarrow SO_4^{-\bullet} + H^+ + Mn_2O_3 \tag{3.8}$$

$$HSO_5^- + 2Mn_3O_4 \rightarrow SO_4^{-\bullet} + H^+ + 3Mn_2O_3 \tag{3.9}$$

In addition, various manganese oxide composites with mixed Mn valence states and different nanostructures, shapes, and surface permeability have been developed to enhance the catalytic reactivity, such as α-Mn_2O_3@α-MnO_2 (Khan et al., 2018a; Saputra et al., 2016) and Mn_2O_3@Mn_5O_8 (Khan et al., 2018b). For example, α-Mn_2O_3@α-MnO_2 calcinated at 500°C has been demonstrated to be a better catalyst in the activation of PMS to remove phenol than α-, β-, γ-, and δ-MnO_2, Mn_2O_3, and Mn_3O_4 (Khan et al., 2018a). This was ascribed to the higher degree of crystallinity, proper size, and mixed valence Mn components. Similar results were obtained for yolk shell Mn_2O_3@Mn_5O_8, which might be due to the mixed valence state and proper particle size (Khan et al., 2018b). In short, to better understand the reactivity of MnO_x, structural and surface physicochemical properties including morphology, surface area, exposed reactive facets, Mn AOS, Mn(III) content, conductivity and oxygen species should be taken into consideration.

Besides the frequently reported radical mechanisms based on $SO_4^{-\bullet}$ and $^{\bullet}OH$, non-radical mechanisms such as $^1O_2$ were also reported to be important in PMS/MnO_x systems. Previous research showed that biogenic MnO_x demonstrated stable and good performance toward phenol degradation, and the reactive oxygen species were $^1O_2$ and $SO_4^{-\bullet}$ (Tian et al., 2018). $^1O_2$ formed upon the self-decomposition of PMS (Eq. (3.10)) (Zhou et al., 2015).

$$HSO_5^- + SO_5^{2-} \rightarrow HSO_4^- + SO_4^{2-} +^1 O_2 \tag{3.10}$$

In addition, different reaction mechanisms were even reported for the same structure of MnO_x in the activation of PMS. For example, Saputra et al. (2013a, 2013b, 2013c) proposed that $SO_4^{-\bullet}$ and $^{\bullet}OH$ were responsible for the degradation of phenol in PMS/Mn_2O_3. However, other researchers demonstrated that only $^1O_2$ was detected in PMS/Mn_2O_3 (Tian et al., 2019). Moreover, Saputra et al. (2016) showed that α-Mn_2O_3@α-MnO_2 can generate free radicals ($SO_4^{-\bullet}$ and $^{\bullet}OH$), while Khan et al. (2018a, 2018b) discovered that besides free radicals, $^1O_2$ was also involved in the reaction. Further research on the reasons for these differences is warranted. However, we noticed that a number of early papers that examined the activation of PMS by MnO_x just proposed the mechanisms without directly identifying the proposed reactive species (Table 1), so it might be necessary to revisit some of these systems to check if the proposed mechanisms were complete.

3.2. *Activation of PDS by MnO_x*

Compared with PMS, there are only a few papers reporting PDS activation by MnO_x (Table 2). MnO_2 has been used to active PDS to remove different contaminants, such as nitrobenzene and phenol (Ahmad et al., 2010; Li et al., 2016; Zhao et al., 2016; Zhu et al., 2019). For example, $SO_4^{-\bullet}$ and $^{\bullet}OH$ were believed to be responsible for the removal of 2,4-dichlorophenol in PDS/α-MnO_2 (Zhao et al., 2016), as shown in Eqs. (3.11)–(3.12) (for $SO_4^{-\bullet}$) and Eqs. (3.3)–(3.4) (for $^{\bullet}OH$). However, Zhu et al. (2019) attributed the degradation of phenol in PDS/β-MnO_2 to a non-radical mechanism (i.e., $^1O_2$). The authors believed that the generation of $^1O_2$ might be due to the direct oxidation or recombination of $O_2^{-\bullet}$ (Eqs. (3.13)–(3.16)). Given the limited research in this area, investigating the reason that different types of MnO_2 led to different reactions might prove important.

$$S_2O_8^{2-} + \equiv Mn(IV) \rightarrow S_2O_8^{-\bullet} + \equiv Mn(III) \tag{3.11}$$

$$S_2O_8^{2-} + \equiv Mn(III) \rightarrow SO_4^{-\bullet} + SO_4^{2-} + \equiv Mn(IV) \tag{3.12}$$

$$2[\equiv Mn(IV) - OH]^{III} + HS_2O_8^- \rightarrow 2[\equiv Mn(IV) - O - O - SO_3]^{II} + 3H^+ \tag{3.13}$$

$$\begin{aligned} &2[\equiv Mn(IV) - O - O - SO_3]^{II} + 4H_2O + S_2O_8^{2-} \\ &\quad \rightarrow 2[\equiv Mn(III) - OH]^{II} + SO_4^{2-} + 2O_2^{-\bullet} + 8H^+ \end{aligned} \tag{3.14}$$

$$\begin{aligned} &[\equiv Mn(IV) - O - O - SO_3]^{II} + O_2^{-\bullet} + +OH^- \\ &\quad \rightarrow [\equiv Mn(III) - OH]^{II} + SO_4^{2-} +^1 O_2 \end{aligned} \tag{3.15}$$

$$2O_2^{-\bullet} + 2H_2O \rightarrow^1 O_2 + H_2O_2 + 2OH^- \tag{3.16}$$

Besides MnO_2, other MnO_x have also been demonstrated to effectively activate PDS, including MnO, Mn(III)(oxyhydr)oxides, and nano zerovalent Mn (Do et al., 2013; Li et al., 2016; Shah et al., 2019). Among three Mn(III)O_x, γ-MnOOH demonstrated better catalytic reactivity than α-Mn_2O_3 and Mn_3O_4 in PDS activation to remove phenol (Li et al., 2016). The authors believed that under neutral and alkaline conditions, $SO_4^{\bullet-}$ and $^{\bullet}OH$ were dominant in phenol removal, while under acidic conditions, the phenol removal was due to the strong oxidation by γ-MnOOH and by an oxidative intermediate formed between PDS and γ-MnOOH. In addition, $SO_4^{-\bullet}$ and $^{\bullet}OH$ were reported to be responsible for the removal of ciprofloxacin in PDS/MnO_x (Shah et al., 2019), with the mechanisms similar to Eqs. (3.11)–(3.12).

3.3. Generation of radicals through different reactions

As discussed above, besides the generation of free radicals (e.g., $SO_4^{-\cdot}$ and $HO^{\cdot}$), non-radical mechanisms have also been observed in recent studies. $SO_4^{-\cdot}$ mainly comes from PMS/PDS activation by low valent MnO_x, while $HO^{\cdot}$ might be generated from either the reaction between $SO_4^{-\cdot}$ and H_2O or OH^- (Eqs. (3.3) and (3.4)) or from the disassociation of PMS (Eq. (3.17)):

$$HSO_5^- \rightarrow HO^{\cdot} + SO_4^{2-} \tag{3.17}$$

${}^1O_2$, an excited state of O_2, is a mild and selective oxidant and is resistant to saturated alcohols (methanol or ter-butanol) (Duan et al., 2018a). The lifetime of ${}^1O_2$ is about 3 μs in water, which is much shorter than that in air (Nosaka and Nosaka, 2017). ${}^1O_2$ has been widely reported to occur in photochemical processes via photoinduced energy transfer to O_2 (Chen and Jafvert, 2010; Nosaka and Nosaka, 2017). Other studies have also shown that ${}^1O_2$ could be produced though non-photo-induced methods (Huang et al., 2019b; Zhu et al., 2019). The generation of ${}^1O_2$ can be summarized in four different reactions: 1) the self-decomposition of PMS (Eq. (3.10)). Studies have shown that the typical triplet signals for ${}^1O_2$ still remained when the reaction was conducted under nitrogen atmosphere, suggesting that ${}^1O_2$ was generated from the decomposition of PMS, not from dissolved oxygen (Khan et al., 2018a); 2) the recombination of $HO^{\cdot}$ (Eq. (3.18)) (Huang et al., 2019b; Li et al., 2019; H. Lin et al., 2019); 3) the decomposition of lattice oxygen (Eq. (3.19)) (Tian et al., 2019); and 4) the energy trapping by surface adsorbed O_2 (Eq. (3.20)) (Y. Huang et al., 2018). A mechanism similar to the last one was also reported in Tian et al. (2018) where the phenol degradation rate constant decreased from 0.106 to 0.03 min^{-1} when the reaction was conducted in air versus in nitrogen atmosphere.

$$2HO^{\cdot} \rightarrow 1/2\,{}^{1}O_2 + H_2O \tag{3.18}$$

$$O_{latt} \rightarrow {}^{1}O_2 \tag{3.19}$$

$$\equiv O_2 \overset{energy}{\rightarrow} O_2^1 \tag{3.20}$$

Superoxide ($O_2^{-\cdot}$) is produced when O_2 accepts an electron (Fernández-Castro et al., 2015). Similar to singlet oxygen, $O_2^{-\cdot}$ has also been shown to be generated by both photochemical (Nosaka and Nosaka, 2017) and non-photochemical processes (Zhu et al., 2019). For SR-AOPs activated by Mn-based materials, $O_2^{-\cdot}$ could be generated through using PMS (Eq. (3.21)) (Fan et al., 2019) or PDS (Eq. (3.14)) (Zhu et al., 2019). In addition, the recombination of $O_2^{-\cdot}$ might produce singlet oxygen (Eq. (3.16)) (Zhu et al., 2019).

$$\equiv Mn(III) + HSO_5^- + H_2O \rightarrow \equiv Mn(II) + O_2^{-\cdot} + 3H^+ + SO_4^{2-} \tag{3.21}$$

3.4. Comparison between PMS and PDS

Different reaction mechanisms were reported in the activation of PMS and PDS even when the same Mn-based materials were employed (Saputra et al., 2013c; Zhu et al., 2019). β-MnO_2 has been utilized to activate PMS to produce $SO_4^{-\cdot}$, $^{\cdot}OH$ and ${}^1O_2$ (Huang et al., 2019b), while the activation of PDS by β-MnO_2 only produced ${}^1O_2$ (Zhu et al., 2019). Similar results were also obtained when PMS/PDS was activated by carbon materials, that is, the reaction of PMS/carbon materials was dominated by free radicals, while that of PDS/carbon materials was based on either ${}^1O_2$ or other nonradical-based mechanisms (Duan et al., 2018b). Compared with the level of understanding of carbon materials used for PMS/PDS activation, the mechanisms of the activation of PMS/PDS by Mn-based materials need future investigations. Also, as mentioned earlier, compared with the activation of PMS by Mn-based materials, there have been only a few papers investigating the activation of PDS by Mn-based materials and the activation mechanisms have not been well studied. Therefore, it is difficult to identify the structural features of Mn-based materials that might have resulted in the difference in the mechanisms.

4. MnO_x hybrids

4.1. Metal oxide-MnO_x hybrids for PMS activation

Numerous studies have showed that the catalytic performance of MnO_x can be enhanced by the incorporation of nanoparticles, mostly due to synergistic effects (Huang et al., 2017). Many metal oxides, including Co_xO_y, Fe_xO_y, Si_xO_y, and Cu_xO_y, have been coupled with MnO_x to enhance their activation of PMS. The most widely used metal oxides are Fe oxides (Table 1), which might be ascribed to several advantages. First, Fe oxides such as magnetite (Fe_3O_4), $ZnFe_2O_4$, and $CuFe_2O_4$ (Du et al., 2018; Wang et al., 2014b; Ye et al., 2018) had magnetic properties so that the hybrid catalysts could be recovered through magnetic separation as a convenient and cost-effective method. It has been shown that although the magnetization saturation value of Fe_3O_4@OMS-2 was only 22 emu/g, much lower than that of pure Fe_3O_4 (107 emu/g), it was still high enough for the catalyst to be separated by an external magnet (Wei et al., 2015). Besides magnetite, $ZnFe_2O_4$ nanoparticles have been viewed as an alternative magnetic material due to the advantages of easy synthesis, high stability under humid air, and low cost, and it had been coupled with MnO_x to activate PMS to remove phenol (Wang et al., 2014b).

Second, the incorporated Fe oxides might be involved in the activation of PMS. For example, Fe can be involved in the reactions shown in Eqs. (4.1)–(4.2) (Liu et al., 2015). However, some studies have demonstrated that Fe oxides themselves were not efficient catalysts for PMS activation because the standard redox potential of Fe^{3+}/Fe^{2+} is only 0.77 V. Therefore, the enhancement might not be due to the additional reactive sites provided by the Fe oxides. Huang et al. (2017) believed that the thermodynamically favorable electron transfer from Fe(II) to Mn(III) was not the reason for the enhanced BPA degradation by PMS/$Mn_{1.8}Fe_{1.2}O_4$ nanospheres, instead, they found that the surface hydroxyl groups were critical in the activation of PMS, and the Fe(III) in $Mn_{1.8}Fe_{1.2}O_4$ was acting like a reservoir for hydroxyl groups and then donated them to the neighboring metal, which favored the activation of PMS.

$$HSO_5^- + \equiv Fe^{II} - OH \rightarrow \equiv Fe^{II} - (O)OSO_3^- + H_2O \tag{4.1}$$

$$\equiv Fe^{II} - (O)OSO_3^- + H_2O \rightarrow SO_4^{-\cdot} + OH^- + \equiv Fe^{III} - OH \tag{4.2}$$

Besides Fe oxides, Cu oxides have also been coupled with MnO_x to activate PMS. Copper oxides have been reported to have much better activity than their homogeneous counterparts (Du et al., 2018), which made them interesting metal oxides in activating PMS. Many Cu oxide catalysts have been used to activate PMS, such as CuO (J. Hu et al., 2017) and $CuFe_2O_4$ (Zhang et al., 2013). It has been shown that compared with pure MnO_x, the incorporation of Cu oxides such as $CuFe_2O_4$@OMS-2 and CuO@OMS-2 would enhance the activation of PMS (Li et al., 2017b; Ye et al., 2018). The authors believed that this is because the incorporation of Cu created more active sites (Eqs. (4.3)–(4.7)) and changed the electronic structure of MnO_x (e.g., increased the abundance of low valent manganese species) (Li et al., 2017b). However, the reduction of Cu(II) ($E_{(Cu(II)/Cu(I))} = 0.15$ V) (Zhang et al., 2013) by HSO_5^- ($E(HSO_5^-/HSO_4^-) = 1.8$ V) (Brandt and Van Eldik, 1995) is thermodynamically unfavorable. Therefore, Zhang et al. later proposed that Cu(II) was transformed to a higher valence copper (i.e., Cu(III)) and proposed the reactions in Eqs. (4.8)–(4.11) (Zhang et al., 2013).

$$Cu(II) + HSO_5^- \rightarrow Cu(I) + SO_5^{-\cdot} \tag{4.3}$$

$$Cu(I) + HSO_5^- \rightarrow Cu(II) + SO_4^{-\cdot} \tag{4.4}$$

$$Cu(I) + HSO_5^- \rightarrow Cu(II) + HO^{\cdot} + SO_4^{2-} \tag{4.5}$$

$$\mathrm{Cu(I) + Mn(IV) \rightarrow Cu(II) + Mn(III)} \tag{4.6}$$

$$\mathrm{Cu(I) + Mn(III) \rightarrow Cu(II) + Mn(II)} \tag{4.7}$$

$$\equiv \mathrm{Cu^{2+}–OH^{-} + HSO_5^{-} \rightarrow {\equiv}Cu^{2+} - (HO)O\ SO_3^{-} + OH^{-}} \tag{4.8}$$

$$\equiv \mathrm{Cu^{2+} - (HO)O\ SO_3^{-} \rightarrow {\equiv}Cu^{3+}–OH^{-} + SO_4^{-\bullet}} \tag{4.9}$$

$$\equiv \mathrm{Cu^{3+}–OH^{-} + HSO_5^{-} \rightarrow {\equiv}Cu^{2+} -^{\bullet}\ OO\ SO_3^{-} + H_2O} \tag{4.10}$$

$$\equiv \mathrm{Cu^{2+} -^{\bullet}\ OO\ SO_3^{-}2H_2O \rightarrow {\equiv}Cu^{2+}–OH^{-} + O_2 + 2SO_4^{-\bullet} + 2H^{+}} \tag{4.11}$$

Co oxides are another group of oxides that has been coupled with MnO_x to activate PMS. Among different transition metal ions (e.g., Mn^{2+}, Fe^{2+}), Co^{2+} demonstrated the best performance in the activation of PMS (Anipsitakis and Dionysiou, 2003, 2004a), and Hu and Long (2016) have reviewed Co-mediated activation of PMS (Hu and Long, 2016). Briefly, Co oxides can provide additional active sites in the activation of PMS, as shown in Eqs. (4.12)–(4.16) (Khan et al., 2017; Yao et al., 2015). In addition, Co(III)/Co(II) redox pairs might be involved in the redox reaction of Mn(IV) and Mn(III), as shown in Eqs. (4.17)–(4.18) (Zhang et al., 2019). However, Co is very toxic, which would inhibit its practical application due to possible health concerns.

$$\equiv \mathrm{Co^{2+} + H_2O \rightarrow {\equiv}CoOH^{+} + H^{+}} \tag{4.12}$$

$$\equiv \mathrm{CoOH^{+} + HSO_5^{-} \rightarrow {\equiv}CoO^{+} + SO_4^{-\bullet} + H_2O} \tag{4.13}$$

$$\equiv \mathrm{Co^{2+} + HSO_5^{-} \rightarrow {\equiv}Co^{3+} + SO_4^{-\bullet} + OH^{-}} \tag{4.14}$$

$$\equiv \mathrm{CoO^{+} + 2H^{+} \rightarrow {\equiv}Co^{3+} + H_2O} \tag{4.15}$$

$$\equiv \mathrm{Co^{3+} + HSO_5^{-} \rightarrow {\equiv}Co^{2+} + SO_5^{-\bullet}H_2O} \tag{4.16}$$

$$\mathrm{Co(III) + Mn(III) \rightarrow Co(II) + Mn(IV)} \tag{4.17}$$

$$\mathrm{Co(III) + Mn(II) \rightarrow Co(II) + Mn(III)} \tag{4.18}$$

Si oxides have also been coupled with MnO_x to activate PMS (Yang et al., 2016; Yang et al., 2017). Yang et al. demonstrated that the reactivity of MnO_x/SBA-15 was higher than bare MnO_x, due to the change in the porous structure, the average valence of Mn, and higher dispersion of MnO_x species formed in/on SBA-15 (Yang et al., 2016).

4.2. Metal oxide-MnO_x hybrids for PDS activation

So far, MnO_x coupled with other metal oxides, such as iron oxides (Fe_2O_3 and Fe_3O_4) and copper oxide (CuO), have been employed to activate PDS. $SO_4^{-\bullet}$ and $^{\bullet}OH$ were believed to be generated in the presence of PDS/metal oxides-MnO_x hybrids. These second metal oxides could play a key role in the activation of PDS. For example, γ-Fe_2O_3 might be involved in the activation of PDS by γ-Fe_2O_3/Mn_3O_4 (Eqs. (4.19)–(4.21)) (Ma et al., 2019b). The authors believed that Mn (II) acted as an electron shuttle and could be used for the regeneration of Fe(II), thus improving the reactivity (Ma et al., 2019b). The authors seemed to suggest that Mn was not directly involved in the reaction; however, as discussed above, this mechanism might also be involved in the activation of PDS. In addition, similar to what has been discussed above about the Fe oxide effects, the incorporation of Fe oxides into MnO_x to activate PDS could possess good magnetic properties (Ma et al., 2019b) to facilitate magnetic separation.

$$\mathrm{S_2O_8^{2-} + Fe(II) \rightarrow SO_4^{-\bullet} + Fe(III) + SO_4^{2-}} \tag{4.19}$$

$$\mathrm{Fe(III) + H_2O \rightarrow Fe(III) + HO^{\bullet} + H^{+}} \tag{4.20}$$

$$\mathrm{Fe(III) + Mn(II) \rightarrow Fe(II) + Mn(III)} \tag{4.21}$$

For Cu oxides, they could also provide additional active sites for the activation of PDS, as shown in Eqs. (4.22)–(4.23) (Ma et al., 2019a).

$$\mathrm{S_2O_8^{2-} + Cu(II) \rightarrow SO_4^{-\bullet} + Cu(III) + SO_4^{2-}} \tag{4.22}$$

$$\mathrm{Cu(III) + H_2O \rightarrow Cu(II) + HO^{\bullet} + H^{+}} \tag{4.23}$$

4.3. MnO_x-carbonaceous material hybrids for PMS activation

MnO_x-carbonaceous material hybrids have also been shown to be effective catalysts for the activation of PMS, such as $MnFe_2O_4$/graphene, γ-MnO_2/reduced graphene oxide, OMS-2/g-C_3N_4, and Mn/g-C_3N_4 (Yao et al., 2014). The advantages of adding these carbonaceous materials can be summarized as follows. First, these materials can prevent the aggregation of MnO_x in order to have higher surface areas and hence more active sites to enhance the reactivity (Yao et al., 2013). Second, zigzag edges and ketonic carbonyl groups (C=O) on the edges of carbon materials could provide additional active sites to facilitate PMS activation (Duan et al., 2015a; Duan et al., 2015b; Yu et al., 2019).

Third, the incorporation of carbonaceous materials could change the distribution of Mn species. It has been shown that the composite of g-C_3N_4 and carbon nanofibers (CNFs) with OMS-2 could increase the abundance of low valent manganese species to enhance the catalytic reactivity (Li et al., 2017a).

Fourth, other properties of the hybrids might have been changed to enhance the reactivity. For example, the chemical and thermal stability of Mn_3O_4 can be enhanced by depositing Mn_3O_4 on reduced-graphene oxides (Ding et al., 2013). CNFs have conductive cores, which might favor faster transfer of electrons for OMS-2/CNFs hybrids (Wang et al., 2019).

The mechanisms of MnO_x-carbonaceous material hybrids might depend on the types of the carbonaceous materials. For example, Li et al. (2017a, 2017b) showed that $SO_4^{-\bullet}$, $^{\bullet}OH$ and $^1O_2$ were not the reason for the contaminant degradation when using OMS-2/g-C_3N_4 to activate PMS, and they proposed that highly active manganese species (e.g., Mn(IV) and Mn(V)) or caged radicals might be generated through the oxidation of Mn(II) and Mn(III) (Li et al., 2017a). However, (Wang et al., 2019) demonstrated that the activation of PMS by OMS-2/carbon nanofiber generated sulfate radicals to remove the contaminants. The reason that different non-metal oxides affected the activation mechanisms should be further investigated.

4.4. Doped MnO_x for PMS activation

A number of studies have shown that the introduction of single ions such as Pt^{+}, Ce^{3+}, Co^{2+}, Fe^{3+}, and Cu^{2+} (Adjimi et al., 2017; Biswas et al., 2015; King'ondu et al., 2011) into the structures of MnO_x can modify their properties, which could enhance their catalytic reactivity in applications like energy and environmental treatment. For example, it has been shown that the incorporation of ruthenium into K-OMS-2 can enhance NO oxidation (Adjimi et al., 2017). Doped MnO_x have also been shown to be good catalysts for the activation of PMS.

It has been reported that the incorporation of 4% Ce into 3D Mn_2O_3 can increase the Mn(III) content, which significantly enhanced the PMS activation to degrade 2,4-dichlorophenol (Tian et al., 2019). The mechanisms of PMS activation by Ce/Mn_2O_3 versus by Mn_2O_3 are different. Only $^1O_2$ was detected in Mn_2O_3, while $SO_4^{-\bullet}$, $^{\bullet}OH$ and $^1O_2$ were detected in the Ce-doped Mn_2O_3 (Tian et al., 2019). The authors believed that the doped Ce could improve the charge transfer ability, which favored the generation of $SO_4^{\bullet -}$ and $^{\bullet}OH$. Moreover, the doped Ce could provide additional active sites, which were also involved in the activation of PMS, as shown in Eqs. (4.24)–(4.25) (Tian et al., 2019). However, overloading of Cerium decreased the reactivity due to the collapse of the structure.

$$\mathrm{HSO_5^{-} + Ce(III) \rightarrow SO_4^{-\bullet} + Ce(IV) + OH^{-}} \tag{4.24}$$

$$\mathrm{HSO_5^{-} + Ce(IV) \rightarrow SO_5^{-\bullet} + H^{+} + Ce(III)} \tag{4.25}$$

Cu(II) is another important dopant since the redox cycle of Cu(II)/Cu(I) might improve the catalytic reactivity. Y. Huang et al. (2018) showed that doping Cu into MnO_2 could significantly enhance the activation of PMS to degrade phenol by providing more active sites and forming a long-range ordered mesoporous structure. Moreover, Co has been incorporated into biogenic MnO_x for enhanced tetracycline degradation (Luo et al., 2019), and the mechanism was similar to that of cobalt oxide-MnO_x hybrids (Eqs. (4.12)–(4.18)).

4.5. *Other Mn-based materials*

Mn-based perovskite oxides, with high oxygen mobility and multivalent Mn, have been shown to be efficient catalysts to activate PMS (Tian et al., 2017). $^1O_2$ rather than $SO_4^{-\bullet}$ and $^\bullet OH$ was reported to be the dominant reactive species in the activation of PMS by $LaMnO_3$ to degrade phenol and ofloxacin (Tian et al., 2017), which might result from the energy trapped by the produced oxygen (Nau and Scaiano, 1996). A recent paper by the same authors demonstrated that the amount of surface oxygen defects was important in the activation of PMS to generate $^1O_2$ (P. Gao et al., 2019). Similar results and mechanisms were observed when using $La_{0.4}Sr_{0.6}MnO_{3-\delta}$ to activate PMS to degrade phenol (Miao et al., 2019). However, $SO_4^{-\bullet}$ and $^\bullet OH$ were demonstrated to be the reactive species to degrade phenol in the activation of PMS by $LaCo_{1-x}Mn_xO_{3+\delta}$ (Miao et al., 2018). The difference in the observed mechanisms between these studies should be further elucidated.

In addition, layered double hydroxides (LDHs) with a hydrotalcite-like structure have been increasingly used in various applications, such as reduction (Liang et al., 2015), catalysis (Liang et al., 2015), and advanced oxidation (Zhao et al., 2018). Among them, Mn-based LDHs (e.g., Co—Mn LDH and Mn—Fe LDH) have been demonstrated to be efficient catalysts to activate PMS (L. Hou et al., 2019). For example, Mn—Fe LDH was observed to rapidly activate PMS to degrade Acid Orange 7, with $SO_4^{-\bullet}$ and $^\bullet OH$ as the reactive species (L. Hou et al., 2019).

5. Factors influencing the reactivity

5.1. *pH effects*

The effects of pH in a wide range (pH 3–12) on the activation of PMS/PDS by different Mn-based catalysts have been investigated. For instance, Jo et al. (2014a) examined pH between 3 and 12 and determined the optimum pH to be at 9. The optimum pH values are different for various studies, varying from pH 2 (Shah et al., 2019), to 5 (Zhu et al., 2019), and to 9 (Jo et al., 2014a). It seems that there is no general trend about the pH effects, most likely due to the following three reasons: first, low pH caused dissolution and hence release of Mn (II) into the aqueous phase, which might change the surface structure of Mn-based materials, resulting in the inhibition of the reactivity. The large amount of protons at low pH might also compete with the Mn-based materials in binding to PMS/PDS to inhibit the catalytic reactivity (Dong et al., 2019).

Second, the interactions between catalysts and PMS/PDS can also affect the reactivity. The pH_{pzc} of Mn-based materials are different, resulting in different surface charges at different pHs. The different surface charges will affect the interaction between the Mn-based materials and PMS/PDS through electrostatic repulsion, which can in turn affect the reactivity (Qu et al., 2019).

Third, the transformation of the radicals at different pH can result in the different pH effects. Sulfate radicals can be depleted by reacting with OH^- to form hydroxyl radicals (Eq. (5.1)) (Ma et al., 2019a). The reduction potential of $HO^\bullet$ is different under different pH, which might affect the reactivity. For example, it has been reported that the reduction potential of $HO^\bullet$ is 1.8 V under neutral pH but 2.7 V in acidic solution (Buxton et al., 1988; S. Wang et al., 2015). Moreover, compared with $SO_4^{-\bullet}$, the lifetime of $HO^\bullet$ is much shorter (30–40 μs vs 20 ns) (Ghanbari and Moradi, 2017; Wang and Wang, 2018), so the conversion of $SO_4^{-\bullet}$ to $HO^\bullet$ might inhibit the degradation of contaminants at higher pH (Ma et al., 2019a). Overall, it is important to control the surface properties of Mn-based catalysts to make them work efficiently within a wide pH range.

$$SO_4^{-\bullet} + HO^- \rightarrow SO_4^{2-} + HO^\bullet \tag{5.1}$$

5.2. *Inorganic ions*

It has been shown that many inorganic ions can inhibit contaminant degradation by PMS/PDS with Mn-based catalysts in two ways: 1) inhibit the adsorption of contaminants on the surface of the catalysts, and 2) compete with contaminants for the sulfate and hydroxyl radicals (Shah et al., 2019).

Carbonate/bicarbonate is one of the most common inorganic anions in water and wastewater. The presence of HCO_3^- might have both inhibition and promotion effects. On the one hand, it could react with both $SO_4^{-\bullet}$ and $HO^\bullet$ to form less reactive carbonate radicals ($CO_3^{\bullet-}$) to decrease the reactivity (Eqs. (5.2)–(5.5)) (Shah et al., 2019). On the other end, it has been shown that HCO_4^-, a moderate oxidant, can be generated in the activation of PDS by HCO_3^- to enhance the reactivity (Jiang et al., 2017).

$$HO^\bullet + CO_3^{2-} \rightarrow HO^- + CO_3^{\bullet-} \tag{5.2}$$

$$SO_4^{-\bullet} + CO_3^{2-} \rightarrow SO_4^{2-} + CO_3^{\bullet-} \tag{5.3}$$

$$HO^\bullet + HCO_3^- \rightarrow CO_3^{\bullet-} + H_2O \tag{5.4}$$

$$SO_4^{-\bullet} + HCO_3^- \rightarrow SO_4^{2-} + CO_3^{\bullet-} + H^+ \tag{5.5}$$

Nitrate (NO_3^-) and nitrite (NO_2^-) are also common in ground water, drinking water and wastewater (Wang and Chu, 2016). Both NO_3^- and NO_2^- have been reported to inhibit the reactivity, which could be ascribed to their reaction with $SO_4^{-\bullet}$ and $HO^\bullet$ (Eqs. (5.6)–(5.8)) (Shah et al., 2019). NO_2^- showed higher inhibition effects than other inorganic ions with the inhibition effects decreasing in the order: $NO_2^- > CO_3^{2-} > HCO_3^- > NO_3^-$. This might be due to the highest second order reaction rates of NO_2^- with $SO_4^{-\bullet}$ and $HO^\bullet$ (Shah et al., 2019).

$$HO^\bullet + NO_2^- \rightarrow HO^- + NO_2^\bullet \quad (k = 8.0 \times 10^9 M^{-1} s^{-1}) \tag{5.6}$$

$$SO_4^{-\bullet} + NO_4^{2-} \rightarrow SO_4^{2-} + NO_2^\bullet \quad (k = 8.8 \times 10^8\ M^{-1}\ s^{-1}) \tag{5.7}$$

$$SO_4^{-\bullet} + NO_3^- \rightarrow SO_4^{2-} + NO_3^\bullet \quad (k = 5.0 \times 10^4\ M^{-1} s^{-1}) \tag{5.8}$$

Chloride ion (Cl^-) is commonly found in different water matrices, such as surface water, groundwater and industrial wastewater (Fang et al., 2012). The influence of Cl^- on SR-AOPs was less than that of other inorganic ions despite its high reaction rates with both $SO_4^{-\bullet}$ and $HO^\bullet$. Liang et al. (2006) found that the degradation of TCE was not influenced when Cl^- was below 0.2 M, and the degradation rate only decreased at $Cl^- > 0.2$ M when Cl^- reacted with $SO_4^{-\bullet}$ and $HO^\bullet$ to produce less reactive chlorine radicals (Eqs. (5.9) and (5.10)) (Shah et al., 2013). The degradation of BPA was even slightly enhanced when the concentration of Cl^- increased from 1 to 10 mM, which was ascribed to the formation of $Cl^\bullet$ during the reaction (H. Lin et al., 2019). The authors believed that $Cl^\bullet$, with a high redox potential of 2.4 V ($Cl^\bullet/Cl^-$), could react selectively with electron rich organic compounds (Shah et al., 2013). $Cl^\bullet$ might also induce the propagation reactions and generate more $SO_4^{-\bullet}$ (Liang et al., 2006) and •OH (Eq. (5.11)) (Shah et al., 2013), which then enhanced the reactivity.

$$HO^\bullet + Cl^- \rightarrow ClOH^{\bullet-} \tag{5.9}$$

$$SO_4^{-\bullet} + Cl^- \rightarrow SO_4^{2-} + Cl^\bullet \tag{5.10}$$

$$Cl^\bullet + H_2O \rightarrow HO^\bullet + H^+ + Cl^- \tag{5.11}$$

5.3. NOM

Natural organic matter (NOM) is ubiquitous in the environment, which might also affect the reactivity of reactive oxygen species. Fulvic acid (FA) is usually selected as a model NOM, because around 70% of NOM is composed of FA in nature (Zhou et al., 2019). As shown in Eqs. (5.12)–(5.13) (Shah et al., 2019), NOM reaction with $HO^{\bullet}$ is more than one order of magnitude faster than that with $SO_4^{-\bullet}$, indicating that the effect of NOM on SR-AOPs should be less than on Fenton and Fenton-like reactions. Therefore, in many practical applications, SR-AOPs would be more advantageous than hydroxyl radical-based AOPs (e.g., Fenton reactions). In general, NOM has been found to either enhance or inhibit the activation of PMS/PDS in degrading contaminants. Similar to that of inorganic ions, the inhibition effect of NOM on SR-AOPs might result from two reasons: 1) NOM might inhibit the adsorption of contaminants on the surface of the catalysts and 2) NOM can compete with contaminants for the sulfate and hydroxyl radicals (Shah et al., 2019). For example, the addition of fulvic acid was reported to inhibit the degradation of Rhodamine B (RhB) (Yao et al., 2015), which might be due to the its competition with RhB for the reactive radicals.

$$HO^{\bullet} + \text{NOM} \rightarrow \text{Products}(k = 2.23 \times 10^8 \text{L(molC)}^{-1}\text{s}^{-1}) \tag{5.12}$$

$$SO_4^{-\bullet} + \text{NOM} \rightarrow \text{Products}\,(k > 6.0 \times 10^6\ \text{L(molC)}^{-1}\text{s}^{-1}) \tag{5.13}$$

In addition, previous research implied that semiquinone radicals generated from hydroquinones, quinones and phenols in NOM might have activated PMS to produce $SO_4^{-\bullet}$ and $HO^{\bullet}$ (Guan et al., 2013), which might have enhanced the reactivity. Indeed, the activation of PMS by TiO_2 under visible light has been found to slightly enhance the degradation of AO7, which might be ascribed to the ability of NOM to act as a natural photosensitizer (Chen et al., 2012). It would be interesting to see if NOM has a positive effect on the activation of PMS/PDS by Mn-based materials, which warrants further research.

5.4. O_2 effect

There are only a few papers investigating the effect of dissolved oxygen on the activity of different Mn-based catalysts, with contradictory findings. For example, it has been shown that the decoloration rate of RhB was not inhibited by bubbling the solution with N_2 to remove O_2 (Yao et al., 2015), indicating that dissolved O_2 might not take part in the catalytic reaction. However, another research demonstrated that under nitrogen atmosphere, the phenol degradation rate constant deceased from 0.106 to 0.03 min^{-1}, suggesting that O_2 in solution was involved in the generation of $^1O_2$ (Tian et al., 2018), as mentioned above in Section 4.5. Therefore, it seems like whether O_2 can affect the reactivity largely depends on the activation mechanism by Mn-based catalysts, and this is an issue for future research to explore.

5.5. Temperature effects

Temperature has been demonstrated to be one of the most important factors in PMS/PDS activation. In general, higher temperature resulted in higher reactivity for the activation of PMS/PDS by Mn-based materials. The correlation between the rate constant and temperature was established by fitting the Arrhenius relationship (Eq. (5.14)),

$$\ln k = \ln \text{A} - E_a/\text{RT} \tag{5.14}$$

where A is the frequency factor, E_a is the activation energy, R is the universal gas constant, and T is the absolute temperature. Eq. (5.14) can be used to calculate the activation energy, as shown in Table 3. For example, when the contaminant is phenol, the lowest E_a is 11.4 kJ/mol when using Mn_2O_3 as the catalyst (Saputra et al., 2013b).

Note that heat has been demonstrated to be a viable approach to activate PMS/PDS (Tan et al., 2012; Waldemer et al., 2007; Zhu et al., 2018b). The details of the activation mechanism have been reviewed in a recent paper (Wang and Wang, 2018). The observation that increasing temperature enhanced the activation of PMS/PDS by Mn-based materials might result from two pathways: (1) thermal activation and (2) Mn-based materials activation. Because thermal activation might be involved in the activation of PMS/PDS at high temperature, the reaction mechanisms might be different from those at room temperature. For example, persulfate radical ($S_2O_8^{\bullet-}$) has been proven to play a key role in the degradation of hexachloroethane by thermal activation of PDS under anaerobic conditions (Zhu et al., 2018a). Thus, when investigating the effect of temperature on the activation of PMS/PDS, both mechanisms should be considered.

5.6. Importance of crystallinity

The extent of crystallinity of MnO_x plays a dominant role in the activation of PMS. Saputra et al. (2012) believed that the crystalline structure of MnO_2 (based on XRD data) was more important than surface area and pore structure in activating PMS for phenol degradation. Huang et al. (2019b) demonstrated that δ-MnO_2 showed the least catalytic reactivity among different phase structures of MnO_2, most likely due to its less crystalline structure. The authors found that δ-MnO_2 was less catalytically reactive than the three tunnel structured MnO_2 even though its surface area was about 6 times larger than that of β-MnO_2. Similar results were also obtained when employing MnO_x in other applications (Kim et al., 2016; Meng et al., 2014; Truong et al., 2012). For instance, (Kim et al., 2016) found that compared with α-, β-, and γ-MnO_2, δ-MnO_2 was the least catalytically reactive in the decomposition of H_2O_2, which was ascribed to its low crystallinity and the exposed low-index planes that have lower surface energies. Truong et al. (2012) revealed that δ-MnO_2 was less catalytically reactive in the electrochemical processes in lithium-air batteries due to its poor crystallinity and small size domains. The importance of catalyst crystallinity was also demonstrated in other metal oxides (Hermanek et al., 2007; Jiang et al., 2005; Nicolaides et al., 2002). For example, it has been discovered that the particle crystallinity prevailed over surface area in H_2O_2 decomposition, as increasing crystallinity of Fe_2O_3 favored its reactivity (Hermanek et al., 2007).

In addition, the crystallinity of MnO_x might affect the activation mechanism of PMS. For example, non-radical mechanisms (e.g., direct electron transfer between PMS-MnO_2 and the substrate) have been reported to be involved in the degradation of bisphenol A when using amorphous MnO_2 to activate PMS (Wang et al., 2018). Huang et al. (2019b) also showed that less crystalline MnO_2 might only produce singlet oxygen, while crystalline MnO_2 would generate $SO_4^{-\bullet}$, $HO^{\bullet}$ and $^1O_2$. As a result, only synthesizing more abundant, low valent Mn-containing catalysts (Li et al., 2017a; Wang et al., 2019) might not be enough to increase the catalytic reactivity. Crystallinity of the catalysts should also be taken into consideration, which provides a guidance to develop cost-effective catalysts for water/wastewater treatment.

It is yet unclear why non-radical mechanisms occur for less crystalline and amorphous MnO_x. It is difficult to systematically characterize and investigate the changes in amorphous MnO_x. Under operating conditions, amorphous MnO_x (AMO) might undergo structural transformation to form active sites, which makes it necessary to examine the material change in real time. Therefore, developing methods to elucidate the evolution of both active sites and reaction intermediates is important.

6. Methodologies used to examine the activation of PMS/PDS by Mn-based catalysts

6.1. Reaction kinetics

There are typically two ways to quantify the reactivity of the catalysts. The first method is based on the ratio of C/C_0 (Saputra et al., 2013a; Saputra et al., 2013c; Saputra et al., 2012; Wang et al., 2018).

Table 3
Activation energies of Mn-based catalysts in contaminant degradation.

Mn-based material	Contaminant	Oxidant	E_a (kJ/mol)	Ref.
α-MnO_2	Phenol	PMS	21.9	(Saputra et al., 2013c)
β-MnO_2	Phenol	PMS	38.2	(Saputra et al., 2014b)
Corolla-like δ-MnO_2	Phenol	PMS	25.3	(Wang et al., 2015b)
Mn_3O_4	Phenol	PMS	38.5	(Saputra et al., 2013a)
Mn_2O_3	Phenol	PMS	11.4	(Saputra et al., 2013b)
α-Mn_2O_3	Phenol	PMS	61.2	(Saputra et al., 2014a)
$ZnFe_2O_4/MnO_2$-100	Phenol	PMS	49.4	(Wang et al., 2014b)
$Mn_2O_3@\alpha$-MnO_2-400	Phenol	PMS	39.9	(Saputra et al., 2016)
BioMnOx	Phenol	PMS	18.0	(Tian et al., 2018)
Mn_3O_4/rGO	Orange II	PMS	49.5	(Yao et al., 2013)
MFe_2O_4	Orange II	PMS	31.7	(Yao et al., 2014)
MFe_2O_4/rGO	Orange II	PMS	25.7	(Yao et al., 2014)
MnO_x/SBA-15	Ibuprofen	PMS	44.4	(Yang et al., 2017)
$Mn_2O_3@Mn_5O_8$	4-Chlorophenol	PMS	32.8	(Khan et al., 2018b)
Mn_3O_4/ZIF-8	Rhodamine B	PMS	39.17	(L. Hu et al., 2017)
γ-Fe_2O_3/Mn_3O_4	Rhodamine B	PDS	25.8	(Ma et al., 2019b)

For example, it has been shown that 100% phenol degradation were achieved for α–MnO_2 in 20 min, while 30 and 50 min were needed for γ–MnO_2 and β–MnO_2, respectively, indicating that α–MnO_2 exhibited the best catalytic reactivity (Saputra et al., 2013c). The second method is based on pseudo-first order reaction rate constants (k) (Huang et al., 2019b; Wang et al., 2018). In order to obtain the k values, the concentration of PMS/PDS should be at least 10 times higher than that of the contaminants. Rate constants (k) for the degradation of the contaminants can be calculated using the pseudo first-order kinetics (Eq. (6.1)).

$$\ln\left(\frac{C}{C_0}\right) = -kt \tag{6.1}$$

where k is the rate constant, C_0 is the initial contaminant concentration, and C is the contaminant concentration at time (t).

Note that the removal of contaminants not only resulted from the catalytic degradation, but also from the adsorption onto the oxides. The amount of contaminants adsorbed on MnO_x depends on the properties of the contaminants (e.g., hydrophobicity or hydrophilicity) and the Mn-based materials (e.g., pH_{pzc}, surface area). Some studies had premixed the contaminants and Mn-based materials for certain time (e.g., 30 min) to reach adsorption equilibrium before starting the experiments (Wang et al., 2014b). Methanol is commonly used to quench the reaction, but the time when methanol was added might affect the observed reactivity. For example, the reaction aliquots could be first filtered and then quenched by methanol addition (Saputra et al., 2013c). In this case, the total removal of the organic contaminants included both the adsorbed amount and the amount catalytically degraded. The adsorbed amount should be subtracted from the total removal if the catalytic reactivity was of interest, otherwise, the calculated catalytic reactivity was overestimated. In other studies, the samples were first mixed with methanol to both quench the radicals and desorb the adsorbed contaminant, and then the mixtures were filtered to obtain the remaining contaminant concentration (Huang et al., 2019b). In this way, the adsorption of organic contaminants was negligible, and the observed removal of the organic contaminants was only due to the catalytic reactivity.

In addition, the first-order reaction rate constants determined from competitive kinetic experiments can be used to calculate the second-order constants of the reaction between the contaminants and $SO_4^{-\bullet}$ or •OH. To do this, a reference compound (R) with known second-order rate constants with $SO_4^{-\bullet}$ and •OH was first selected. Then, the unknown second-order rate constants of the target compound (UC) with $SO_4^{-\bullet}$ or •OH were calculated based on Eqs. (6.2) and (6.3). Using this approach, the second order reaction rates of sulfamethoxypyridazine with $SO_4^{-\bullet}$ or •OH were calculated to be 2.73×10^{10} and $2.22 \times 10^{10}\ M^{-1}\ s^{-1}$ (Y.-q. Gao et al., 2019).

$$k_{T,UC} - k_{d,UC} = \frac{k_{SO_4^{-\bullet},UC}}{k_{SO_4^{-\bullet},R}}(k_{T,R} - k_{d,R}) \tag{6.2}$$

$$k_{T,UC} - k_{d,UC} = \frac{k_{\bullet OH,UC}}{k_{\bullet OH,R}}(k_{T,R} - k_{d,R}) \tag{6.3}$$

where $k_{T,UC}$ and $k_{T,R}$ are the pseudo-first order rate constants of the target compound and the reference compound when UV was used to activate PMS/PDS to produce $SO_4^{-\bullet}$ and •OH; $k_{d,UC}$ and $k_{d,R}$ are the pseudo-first order rate constants of the target compound and the reference compound under UV irradiation alone; $k_{SO_4^{-\bullet},\ UC}$ and $k_{SO_4^{-\bullet},\ R}$ are the second order rate constants of the target compound and the reference compound with $SO_4^{-\bullet}$, respectively; and $k_{\bullet OH,\ UC}$ and $k_{\bullet OH,\ R}$ are the second order rate constants of the target compound and the reference compound with •OH, respectively.

6.2. *Scanning electron microscopy (SEM) and transmission electron microscopy (TEM)*

SEM and TEM are two essential instruments to characterize Mn-based materials. SEM can be used to examine the surface morphology of the materials, both before and after the catalytic reaction. For example, it has been shown that the irregular flake shape of γ-MnO_2 and the fibrous morphology of OMS-2 could still be observed in the used catalysts, indicating that the structures of the catalysts remained unchanged during the reaction (J. Xie et al., 2018). SEM coupled with energy-dispersive X-ray (EDS) can be employed for the elemental analysis or chemical characterization of the samples. EDS elemental mapping images can illustrate the distribution of the elements, which are particularly important for doped MnO_x (Fan et al., 2019; Luo et al., 2019; Ma et al., 2019b; Tian et al., 2019; Zhang et al., 2019). For instance, it has been reported that Fe and Mn were uniformly dispersed in the inner and outer shells of $Fe_3O_4@MnO_2$ based on the elemental mapping (Fig. 1) (Zhang et al., 2016), suggesting the successful synthesis of ball-in-ball hollow spheres.

Similar to SEM, TEM has also been used to show the morphology of Mn-based materials (Khan et al., 2017). In addition, high resolution TEM (HRTEM) can be employed to analyze the size and crystallinity of Mn-based materials. For example, HRTEM images showed clear interplanar distances for α-, β-, and γ-MnO_2, indicating that these three MnO_2 were highly crystalline (Fig. 2), whereas δ-MnO_2 did not display clear interparticle boundaries, suggesting it was less crystalline (Huang et al., 2019b).

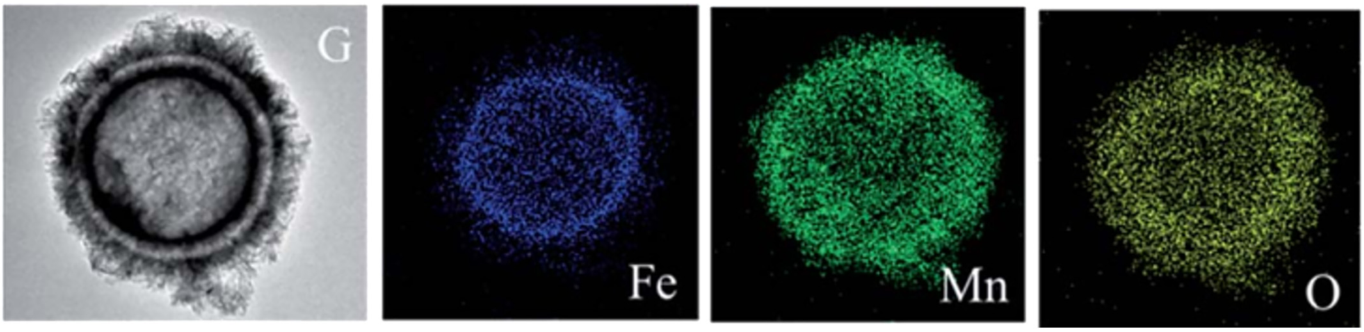

Fig. 1. Images of the elemental mapping of $Fe_3O_4@MnO_2$ (Zhang et al., 2016).

6.3. XRD

When examining the activation of PMS/PDS by Mn-based materials, XRD can be employed to (1) identify the phase structure of MnO_x and (2) illustrate the crystallinity of the materials. For example, different phase structures of MnO_2 were synthesized to test the activation of PMS (Fig. 3). The XRD peaks agreed well with the patterns in the inorganic crystallographic database, with α-MnO_2 (JCPDS 29-1020), β-MnO_2 (JCPDS 24-0735), γ-MnO_2 (JCPDS 14-0644) and δ-MnO_2 (JCPDS 80-1098), indicating different phase structures of MnO_2 were obtained. In addition, XRD can be used to illustrate the extent of crystallinity of Mn-based materials. β-MnO_2 showed high and narrow peaks (Fig. 3), suggesting it was well crystalline, while peaks of δ-MnO_2 are broad and unclear, suggesting it was less crystalline. Crystallinity has been shown to be an important factor that determined the catalytic reactivity (Section 5.6).

XRD can also be used to analyze the distribution of doped elements in MnO_x. For example, XRD spectra showed that MnO_x doped with different amounts of Ce were identified to be a typical cubic phase (Mn_2O_3) and no diffraction peaks of cerium oxide were found, suggesting that Ce was successfully incorporated into the crystalline structure (Tian et al., 2019).

In addition, the particle size of Mn-based materials can be estimated from the broadening of the characteristic peaks in the XRD spectra by applying the Scherrer formula (Vikesland et al., 2007). Using this approach, the particle size of OMS-2 was calculated to be 11 nm for the (211) peak on the XRD data (Luo et al., 2015).

$$d_{XRD} = \frac{K\lambda}{b\cos\theta}\text{(Scherrer formula)} \qquad (6.4)$$

where K is the shape factor, λ is X-ray wavelength, b is corrected line broadening at half of the maximum intensity (FWHM), and θ is the bragg angle.

6.4. Quenching tests

Quenching agents have been widely used to identify radicals. For free radical mechanisms, methanol or ethanol was usually used to quench both sulfate and hydroxyl radicals. Tert-butanol (TBA) was commonly used to quench hydroxyl radicals since its reaction with $^{\bullet}OH$ is faster than that with $SO_4^{-\bullet}$ (Table 4). In order to obtain the relative contributions of $SO_4^{-\bullet}$ and $^{\bullet}OH$ to the compound degradation, the amount of TBA should be carefully calculated so that (1) the *ck* value of $^{\bullet}OH$ with TBA should be ≥10 times greater than that of $^{\bullet}OH$ with the compound to ensure the majority of $^{\bullet}OH$ has been quenched; and (2) the *ck* value of $SO_4^{-\bullet}$ with the compound should also be ≥10 times greater than that of $SO_4^{-\bullet}$ with TBA to ensure that $SO_4^{\bullet-}$ reacts predominantly with the compound. (Here *c* is the concentration of the compound, and *k* is the second order reaction rate of the probe with $SO_4^{-\bullet}$ or $^{\bullet}OH$). The unknown second-order reaction constants of contaminants with $SO_4^{-\bullet}$ or $^{\bullet}OH$ can be calculated through Eqs. (6.2)–(6.3).

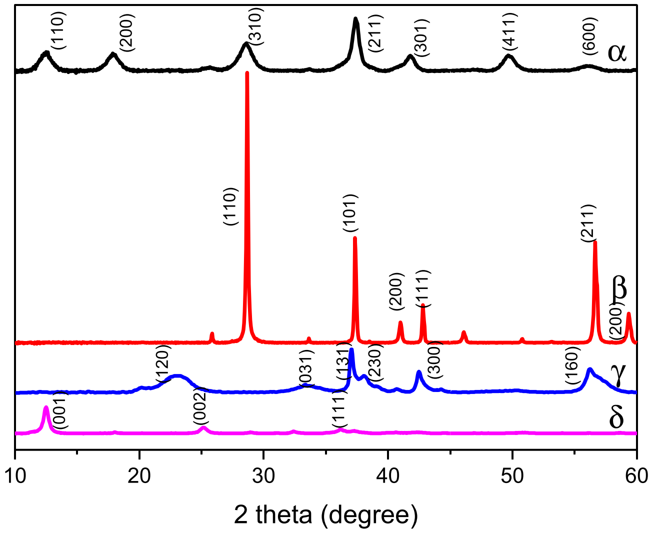

Fig. 3. XRD patterns of different structures of MnO_2 (Huang et al., 2019b).

Furfuryl alcohol (FFA) and NaN_3 are commonly used to identify singlet oxygen. However, it should be noted that FFA can also react with $^{\bullet}OH$, and NaN_3 can react with both $SO_4^{\bullet-}$ and $^{\bullet}OH$ (Table 4); thus,

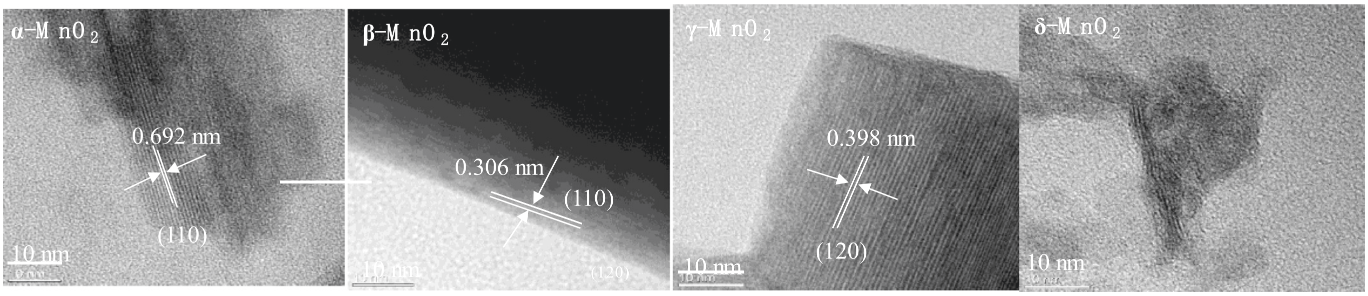

Fig. 2. HRTEM images of different structures of MnO_2 (Huang et al., 2019b).

Table 4
The second order reaction rate constants of different quenching agents with various radicals.

Quenching agent	$SO_4^{-\bullet}$ ($M^{-1} s^{-1}$)	$^{\bullet}OH$ ($M^{-1} s^{-1}$)	$^1O_2$ ($M^{-1} s^{-1}$)	$O_2^{\bullet-}$ ($M^{-1} s^{-1}$)
Methanol	3.2×10^6 (Zou et al., 2014)	9.7×10^8 (Zou et al., 2014)	–	–
Ethanol	3.5×10^7 (Huang et al., 2017)	1.9×10^9 (Huang et al., 2017)	–	–
Tert-butanol (TBA)	4.0×10^5 (Huang et al., 2017)	6.0×10^8 (Huang et al., 2017)	–	–
FFA	–	1.5×10^{10} (Zhou et al., 2015)	1.2×10^8 (Ding et al., 2015)	–
NaN_3	2.5×10^9 (Zhou et al., 2015)	1.2×10^{10} (Zhou et al., 2015)	2×10^9 (Khan et al., 2018a)	–
1,4-Benzoquinone	1.2×10^9 (Criquet and Leitner, 2015)	1×10^8 (Criquet and Leitner, 2015)	–	9.6×10^8 (Bandara and Kiwi, 1999)
Chloroform	–	5.4×10^7 (Smith et al., 2006)	–	3.0×10^{10} (Pan et al., 2018)

the inhibition by FFA or NaN_3 can result from their reaction with not only $^1O_2$, but also $SO_4^{-\bullet}$ and $^{\bullet}OH$. Therefore, the observation that the inhibition effect by NaN_3 or FFA is larger than that by ethanol or methanol does not guarantee that $^1O_2$ is the dominant reactive species. It has to be coupled with other methodologies such as Electron spin resonance (ESR) (details in Section 6.5).

Chloroform ($CHCl_3$) is frequently employed as a quenching agent for $O_2^{\bullet-}$ (Pan et al., 2018). Similar to the discussion about FFA and NaN_3, chloroform can also react with $^{\bullet}OH$ (Table 4), indicating that the inhibition by chloroform might not only result from $^1O_2$, but also from $^{\bullet}OH$. Therefore, additional methods are warranted to identify $O_2^{\bullet-}$.

Moreover, the properties of the contaminants might affect the observed inhibition effects by ethanol and TBA. For instance, it has been shown that the inhibition effect of TBA on BPA degradation was larger than that of EtOH (Huang et al., 2017), which is different from most other results reported. This might be because (1) TBA has higher viscosity than EtOH, resulting in stronger shielding of the bonding site (Du et al., 2018); and (2) BPA is hydrophobic and hence has stronger affinity for the catalyst surface than EtOH (Huang et al., 2017). Therefore, the contaminants as chemical probe compounds should be carefully selected to better understand the mechanisms or additional experiments should be conducted to illustrate the dominant mechanism(s) involved.

6.5. Electron spin resonance (ESR)

ESR have been widely used to identify the reactive species in radical-based reactions. 5,5-dimethylpyrroline-N-oxide (DMPO) is a commonly used spin trap for $SO_4^{-\bullet}$ and $^{\bullet}OH$. The characteristic peaks of DMPO-$^{\bullet}OH$ (hyperfine splitting constants of $a_N = a_H = 14.9$ G) and DMPO- $SO_4^{-\bullet}$ (hyperfine splitting constants of $a_N = 13.2$ G, $a_H = 9.6$ G, $a_H = 1.48$ G, and $a_H = 0.78$ G) are shown in Fig. 4a. 2,2,6,6-tetramethyl-4-piperidinol (TMP) is a commonly used spin trap for $^1O_2$. The characteristic peaks of TMP-$^1O_2$ are the triplet signals (1:1:1), as shown in Fig. 4b.

Studies also reported a narrow seven-line (1,2,1:2:1:2:1) spectrum as the signal for 5,5-dimetphylpyrroline-(2)-oxyl-(1) (DMPOX), which was the oxidation product of DMPO by strong oxidizing substances such as $SO_4^{-\bullet}$ and $^{\bullet}OH$ (Du et al., 2018; Rosen and Rauckman, 1980; M. Xie et al., 2018). Therefore, the presence of DMPOX signals by themselves did not indicate $SO_4^{-\bullet}$ and $^{\bullet}OH$ were absent (Fontmorin et al., 2016; Maeno et al., 2015), but suggested that the rate of DMPO oxidation might be faster than its rate of trapping radicals (M. Xie et al., 2018). Quenching agents (e.g., EtOH and TBA) were then added to observe the change in the intensity of the DMPOX signal, which can indirectly demonstrate the relative contributions of $SO_4^{-\bullet}$ and $^{\bullet}OH$. For example, Xie et al. observed that the DMPOX signal decreased more in intensity by ethanol than by TBA (Fig. 5), indicating that $SO_4^{-\bullet}$ was the main radical species with minor $^{\bullet}OH$ contributions (M. Xie et al., 2018).

In addition, based on the ESR peak intensity, the evolution of different radical species at different reaction times can be obtained. For example, it has been shown that in the beginning of the reaction ($ZnFe_2O_4/MnO_2$ to activate PMS), only $^{\bullet}OH$ formed (1 min). After that, both $SO_4^{-\bullet}$ and $^{\bullet}OH$ formed and the intensity of DMPO-$SO_4^{-\bullet}$ increased as the reaction continued up to 30 min (Wang et al., 2014b). Following that, only signals of DMPO-$^{\bullet}OH$ remained, similar to the observation at the beginning of the reaction, indicating that $^{\bullet}OH$ played an important role at the beginning and late stages of the reaction.

As shown in Tables 1 and 2, some of the earlier papers did not recognize the importance of $^1O_2$. It is unknown if this was because $^1O_2$ was not formed in those systems or just because the authors did not consider its possible formation. More recent papers did investigate the role of $^1O_2$ and showed that it was important for certain Mn-based materials (Khan et al., 2018a; Khan et al., 2018b). Therefore, it might be useful to revisit some systems published earlier to better understand the involved reactive species.

However, the formation of TMPO signals themselves does not necessarily indicate the formation of $^1O_2$. It has been suggested that the generation of TMP radical cations ($TMP^{\bullet+}$) by an excited

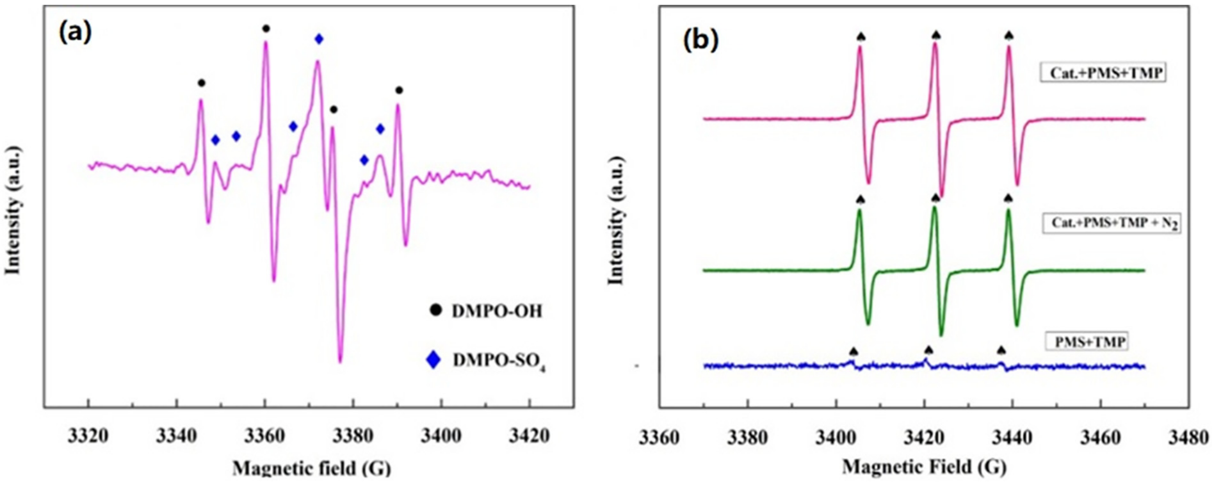

Fig. 4. ESR spectra for different radicals (Khan et al., 2018a).

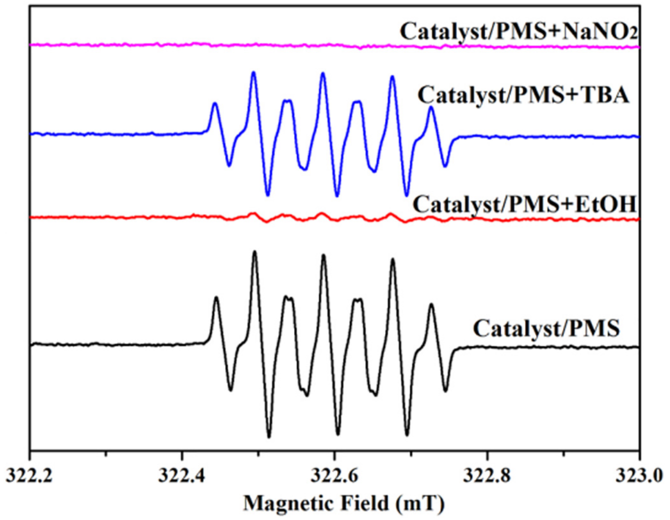

Fig. 5. ESR spectra of PMS activation by Co doped g-$C_3N_4$with/without quenching agents (M. Xie et al., 2018).

photosensitizer might undergo deprotonation and reaction with molecular oxygen to form TMPO signals (Nardi et al., 2014; Yun et al., 2018). Therefore, additional experiments, such as isotope effect experiments, are warranted to see if $^1O_2$ exists in the system, even when TMPO signals are observed.

6.6. Electrochemical methods

Electrochemical methods are helpful in investigating reaction mechanisms. Among them, cyclic voltammogram (CV) has been often used because it can be employed to observe electron transfer properties and redox behavior. CV data can show the current density and reductive capability of Mn-based materials. For example, it has been shown that α-Mn_2O_3@α-MnO_2-500 demonstrated sharp oxidation/reduction cycles due to the existence of mixed valence states of Mn(IV) and Mn(III) in the catalyst (Khan et al., 2018a), verifying its effective redox property during the activation of PMS. CV has also been used to demonstrate that Ce substituted Mn_2O_3 had higher current density and greater reductive capability (Fig. 6a) (Tian et al., 2019).

Electrochemical impedance spectroscopy (EIS) serves as the technique of choice to evaluate the charge transfer resistance in Mn-based catalysts. Lower charge resistance has been reported to be a key factor affecting the catalytic reactivity of crystalline MnO_2 (Huang et al., 2019b). For the Nyquist plots obtained through EIS, the smaller the semicircle diameter within the high frequency region, the better the charge transfer property (Fig. 6b), which would favor the activation of PMS/PDS.

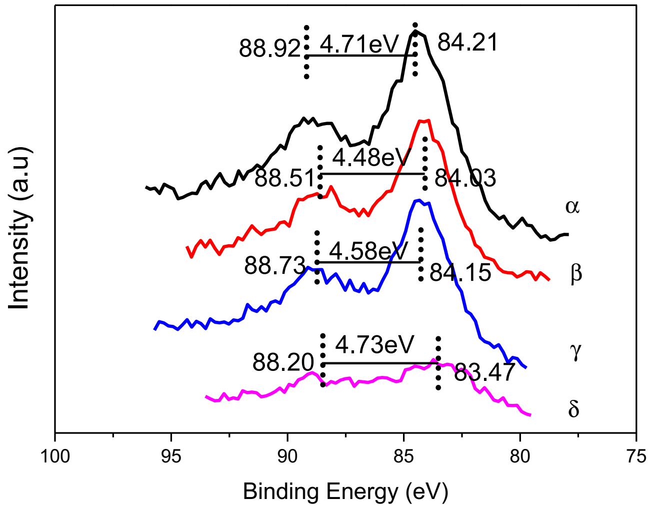

Fig. 7. Mn 3s XPS spectra of different structured MnO_2 (Huang et al., 2019b).

6.7. X-ray photoelectron spectra (XPS)

XPS has been widely utilized to characterize the bonding environment in materials. For instance, XPS has been employed to obtain the changes in the Mn valence of Mn-based catalysts before and after reaction (Khan et al., 2018a). The Mn 3s multiplet splitting (MS) method is commonly used (Gopi et al., 2017; Peluso et al., 2008; Selvakumar et al., 2018; Sun et al., 2013; Wan et al., 2015; X. Xie et al., 2018), where the decrease in the energy separation between the 7S and 5S multiplets is correlated to the increase in the Mn oxidation state (Bagus et al., 2004; Ilton et al., 2016). The Mn average oxidation state (AOS) can also be obtained through the Mn3s multiplet splitting spectra method based on Eq. (6.5). For example, the AOS for α-, β-, γ-, and δ-MnO_2 is 3.63, 3.89, 3.77, and 3.61, respectively (Fig. 7), based on the above method.

$$AOS = 8.95\text{–}1.13\Delta Es \quad (6.5)$$

where ΔEs is the energy difference between the main peak and its

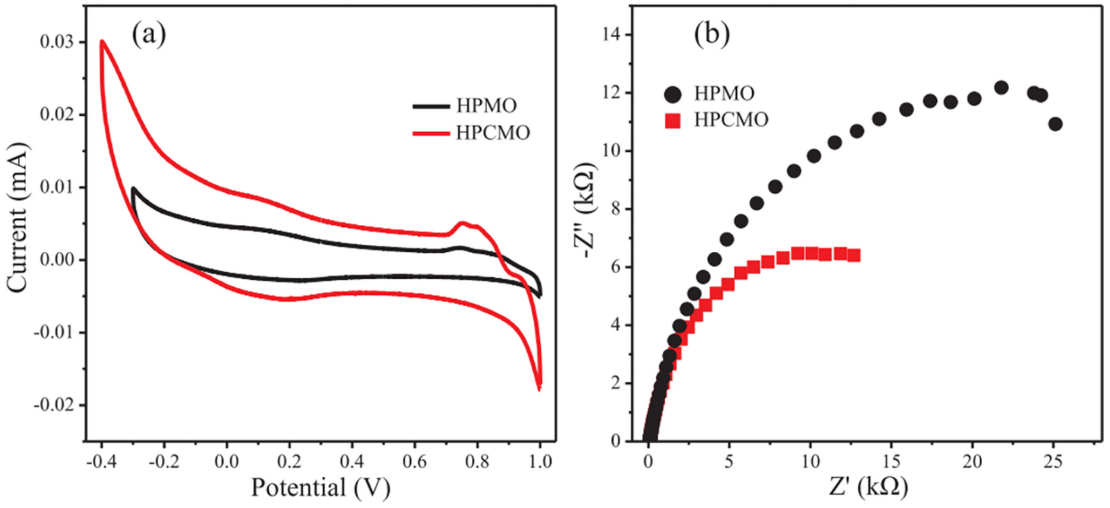

Fig. 6. (a) CV plots of 3D Mn_2O_3 (HPMO) and the Ce substituted 3D Mn_2O_3 (HPCMO); (b) Nyquist plots of HPMO and HPCMO electrodes (Tian et al., 2019).

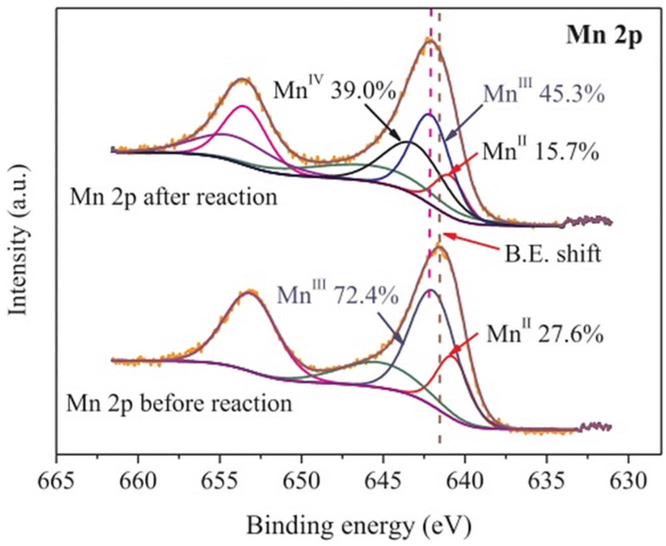

Fig. 8. XPS spectra of Mn2p in manganese/magnetite/graphene oxide hybrid particles before and after the reaction (Du et al., 2018).

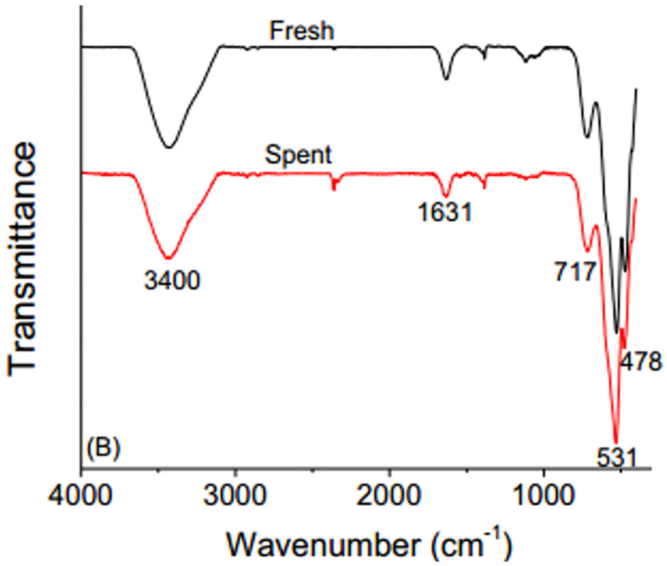

Fig. 9. FTIR spectra of the fresh and used OMS-2 catalyst (Luo et al., 2015).

satellite in Mn 3 s (Wan et al., 2015).

In addition, Mn_{3p}, Mn_{3s}, and $Mn_{2p_{3/2}}$ XPS spectra can be used to obtain the abundance of Mn(II), Mn(III), and Mn(IV) on the manganese oxide surface, which can then be used to help understand the reaction mechanism of PMS/PDS activation by Mn-based materials. For example, it has been shown that the atomic ratio of surface Mn(IV) increased after the reaction, while that of Mn(II) and Mn(III) decreased based on Mn2p (Fig. 8), indicating the valence transformation during the activation of PMS by the Mn-based materials (Du et al., 2016).

XPS O 1s spectra can also be employed to identify the types of surface oxygen species on Mn-based catalysts. The high binding energy peak (533.0 eV) was assigned to the adsorbed molecular water, the medium binding energy between 531.0 eV and 532.0 eV was assigned to surface adsorbed O_{sur} species, while the low binding energy between 529.0 eV and 529.8 eV was attributed to lattice oxygen O_{latt} species. For example, it has been shown that the amount of O_{latt} species in Mn-based catalysts decreased after the activation of PMS (Tian et al., 2019), indicating that O_{latt} was involved in the generation of $^1O_2$.

Note that the detailed XPS analysis methods should be reported to understand how the distribution of Mn(II), Mn(III) and Mn(IV) species was calculated. Only relying on the reported binding energies of different Mn species might not be sufficient because the measured binding energy of the same Mn species may be different in various labs. For example, in the NIST XPS database, the binding energies of MnO_2 obtained from different labs are different, e.g., 50.20, 48.30, and 49.50 eV. Therefore, it is important to obtain the XPS spectra of the standard oxides while measuring the unknown Mn oxide samples, and then fit the spectra of the unknown samples based on those of the standard oxides. Currently, the most rigorous method for determining the Mn oxidation states is to first fit three standard monovalent Mn oxides to obtain the fitting parameters, and then use the obtained fitting parameters to fit the unknown MnO_x samples (Cerrato et al., 2010; Ilton et al., 2016; Shaikh et al., 2016).

6.8. Attenuated total reflection-Fourier transform infra-red (ATR-FTIR)

FTIR has proved to be valuable for the characterization of surface species on Mn-based materials. First, ATR-FTIR can be used to analyze the functional groups on the Mn-based materials. For example, The peaks at around 3430 and 1630 cm^{-1} can be attributed to the stretching and bending vibrations of hydroxyl groups, while the peaks at around 717, 531, and 478 cm^{-1} can be attributed to the vibration of the MnO_6 octahedral framework (Fig. 9) (Luo et al., 2015).

Second, ATR-FTIR can be used to detect the adsorption peaks to understand the catalysis mechanism. It has been shown that the peak intensity at 1247 cm^{-1} (the O—S stretching vibration of HSO_5^-) greatly decreased after the addition of Mn_3O_4-MnO_2 into PMS, suggesting that HSO_5^- was decomposed (Z. Zhao et al., 2017). Moreover, a blue shit of 31 cm^{-1} was observed for the broad adsorption band at 3356 cm^{-1} (i.e., the O—H stretching vibration of the adsorbed water molecules) and the band width became narrower, indicating that the HSO_5^- replaced the hydroxyl groups on the surface of Mn_3O_4-MnO_2 (Fig. 10) (Z. Zhao et al., 2017).

6.9. Isotope experiments

Besides quenching agents (FFA or NaN_3) and ESR, $^1O_2$ can be confirmed by the isotope method. $^1O_2$ exhibits a solvent kinetic isotopic effect as the lifetime of $^1O_2$ in D_2O is longer than that in H_2O (Merkel et al., 1972). This in turn would enhance its oxidative reactivity in D_2O. The reaction rate constant of a compound with $^1O_2$ in the solution containing D_2O at the molar fraction of x_{D_2O}. ($k_{obs,\ H_2O,\ D_2O_{mix}}$) can be

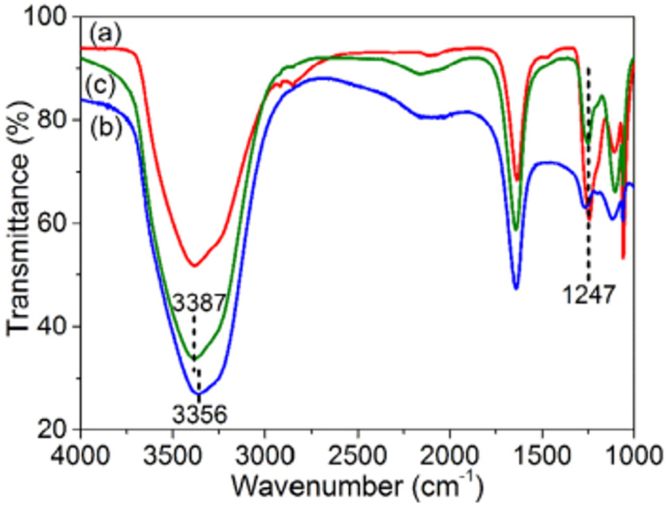

Fig. 10. ATR-FTIR spectra of (a) PMS solution alone; (2) Mn_3O_4-MnO_2 suspension and (c) the mixture of PMS solution and Mn_3O_4-MnO_2 suspension (Z. Zhao et al., 2017).

calculated based on Eq. 6.6 (Jiang et al., 2017):

$$k_{obs,H_2O,D_2O_{mix}} = \frac{k_{H_2O}\bullet k_{obs,H_2O}}{x_{H_2O}.k_{H_2O} + x_{D_2O}.k_{D_2O}} \tag{6.6}$$

where k_{H_2O} and k_{D_2O} are the quenching rate constants of $^1O_2$ by H_2O ($2.5 \times 10^5\,M^{-1}\,s^{-1}$) and D_2O ($1.6 \times 10^4\,M^{-1}\,s^{-1}$), and $k_{obs,\ H_2O}$ is the reaction rate constant of the compound with $^1O_2$ in H_2O.

Using this approach, Zhu et al. (2019) showed that the reactivity of phenol degradation in D_2O by β-MnO_2/PDS was higher than that in H_2O at pH 6.5, indicating that $^1O_2$ was generated. In addition, Jiang et al. (2017) demonstrated that the rate constant of acetaminophenen oxidation was only slightly increased when 50% H_2O was replaced by D_2O, suggesting that $^1O_2$ was not the main reactant in the removal of acetaminophenen. The authors also found that the degradation rate constant of FFA in 50% D_2O ($0.257\,h^{-1}$) was lower than the value ($0.333\,h^{-1}$) calculated based on Eq. 6.6, indicating that there were other reactive species in the reaction that might not have kinetic solvent isotopic effects. Such information can be used to better understand the reaction mechanisms.

7. Common overlooks in the experimental design

7.1. Oxidant versus catalyst for oxidation

As mentioned earlier, Oxone is usually used as the source for PMS but its addition significantly lowers the solution pH. Under acidic conditions, the direct oxidative reactivity of MnO_x toward contaminants will be greatly enhanced (Zhang et al., 2008). In fact, the direct oxidation of MnO_x has been widely investigated in the past four decades (J. Huang et al., 2018; Stone, 1987; Taujale et al., 2016; Zhang and Huang, 2005; Zhang et al., 2015), and has been reviewed in previous research (Remucal and Ginder-Vogel, 2014). Despite this body of knowledge, we surprisingly found that the solution pH of the control experiments for the activation of PMS (Oxone) was not adjusted accordingly in a number of early papers. Therefore, although a significant portion of contaminant degradation might be due to the direct oxidation by MnO_x under the acidic conditions upon Oxone addition, such contribution was not considered in these studies because the control experiments for the degradation of the contaminant by the MnO_x was conducted under near neutral pH, under which the direct oxidation by MnO_x was negligible during the reaction time period (Table 1).

Such a neglect might have made the reactivity quantification less accurate. For example, the addition of 2 g/L Oxone into the solution without buffer would lower the pH to around 2.41 (Saputra et al., 2013c), under which direct oxidation of contaminants by MnO_2 should have been greatly enhanced (Taujale et al., 2016; Zhang and Huang, 2003). Indeed, Huang et al. (2019b) showed that the direct oxidative reactivity at pH 3.07 by the MnO_2 accounted for 25.2, 7.4, 34.1, and 94.5% of the total reactivity of α-MnO_2, β-MnO_2, γ-MnO_2, and δ-MnO_2, respectively, suggesting that direct oxidation played a substantial role in the total degradation under acidic conditions, especially for δ-MnO_2, and the observed oxidation reactivity in many papers was in fact a sum of both catalytic oxidation by PMS/MnO_2 and direct oxidation by MnO_2.

In addition, previous research showed that the catalytic reactivity (should be total reactivity instead) followed the trend: $Mn_2O_3 > MnO > Mn_3O_4 > MnO_2$ (Saputra et al., 2013b). However, our recent results showed that the catalytic reactivity of MnO_2 was higher than that of Mn_2O_3 when taking direction oxidation into consideration, and the direct oxidative reactivity of Mn_2O_3 also played a dominant role in its total reactivity. Thus, the direct oxidative reactivity might also have contributed to the observed total reactivity in a number of published work (Table 1).

The contradictory results reported in some of the XPS data analysis might be also ascribed to the neglect of the contribution of direct oxidation. For example, some showed that the surface Mn(III) on MnO_x was partially transformed to Mn(IV) after the reaction in the PMS-MnO_x system (Khan et al., 2018a), while others showed that the surface Mn (IV) on MnO_x was partially transformed to Mn(III) (Luo et al., 2015). However, the changes were all simply attributed to the catalytic reactivity itself. We believe that the contradictory results not only came from the contribution of catalytic reactivity, but also from direct oxidative reactivity. Previous research using XPS showed that the direct oxidation of phenol, aniline and triclosan by MnO_2 resulted in increasing contents of Mn(II) and Mn(III) but a decreasing content of Mn (IV) (Shaikh et al., 2016). Whereas in the catalytic reaction by MnO_x, the abundance of Mn(II) and Mn(III) decreased and that of Mn(IV) increased (Du et al., 2018; J. Xie et al., 2018). Therefore, the changes in the abundance of surface Mn species after the reaction rely on the relative contributions of direct vs. catalytic oxidation.

Given the above discussion, one important question to answer in the activation of PMS/PDS under acidic conditions is the role of MnO_x. Recent results showed that under acidic conditions, the major role of δ-MnO_2 was an oxidant, while that of β-MnO_2 was a catalyst (Huang et al., 2019b). The results seemed to support that the extent of crystallinity of MnO_x determined if they acted as oxidants or catalysts under acid conditions. Previous research showed similar results when using MnO_x to activate H_2O_2. Sabri et al. (2018) demonstrated that the thermodynamic stability of MnO_x was the dominant factor in determining the catalytic versus direct oxidation of H_2O_2. It has been shown that as an ideal catalyst, MnO_x must accept electrons transiently rather than permanently; however, if electron transfer to Mn is fast and complete, MnO_x would become a chemical oxidant instead (Sabri et al., 2018). Therefore, future studies should aim to examine the role of MnO_x in the activation of PMS in order to develop more efficient catalysts, especially when the reactions are conducted at acidic conditions.

7.2. Buffers

Buffers have been often used to maintain the solution pH when Oxone was added. For example, borate buffer has been used to control the pH between 8–10 (Zhou et al., 2015). However, the buffer employed in the PMS-MnO_x system should be carefully selected because it might affect the reactivity. Previous studies showed that Good's buffers, such as MOPS and HEPES, were not suitable for the systems because they could scavenge the reactive oxygen species, such as •OH and $O_2^{\bullet-}$ (Fang et al., 2013). For example, the rate constant for the reaction between •OH and HEPES buffer was reported to be $5.1 \times 10^9\,mol^{-1}\,s^{-1}$ (Hicks and Gebicki, 1986). Therefore, adequate buffers should be employed in order to accurately quantify the reactivity. Phosphate buffer is usually used to control the pH in the range of 5.6–8. However, phosphate has strong affinity to surface hydroxyl groups, which could inhibit the interaction with PMS (Khan et al., 2018a). In addition, the produced sulfate and hydroxyl radicals can react with HPO_4^{2-} to produce weaker radicals ($HPO_4^{\bullet-}$) (Eqs. (7.1) and (7.2)), which would decrease the reactivity (Maruthamuthu and Neta, 1978).

$$SO_4^{-\bullet} + H_2PO_4^{2-} \rightarrow SO_4^{2-} + HPO_4^{\bullet-} \tag{7.1}$$

$$\bullet OH + H_2PO_4^{2-} \rightarrow OH^- + HPO_4^{\bullet-} \tag{7.2}$$

Some researchers preferred not to use any buffer in the reaction systems to avoid potential interference. In these cases, the pH of the control experiments (MnO_x + contaminants) should be carefully adjusted to the same value as the real experimental conditions (MnO_x + PMS + contaminants). Otherwise, the importance of the direct oxidation by the MnO_x might not be accounted for.

7.3. Reagent addition sequence

The addition sequence of the reagents (e.g., PMS, catalyst and chemical probes) might also affect the observed reactivity. As shown in

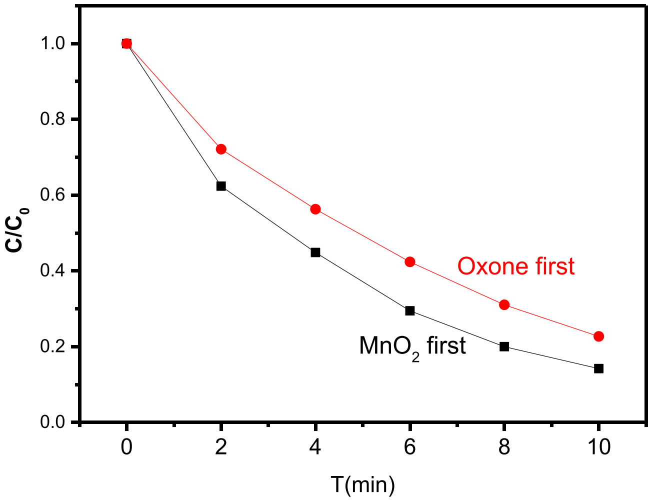

Fig. 11. The effect of reagent-addition order on BPA degradation kinetics. Reaction conditions: BPA 6 μM, MnO_2 0.05 g/L, Oxone 1 mM, pH = 3.

a few papers (J. Hu et al., 2017; Ren et al., 2015), the authors added Oxone and organic compounds first, and then adjusted the pH to a specific value. After that, the reaction was initiated by adding MnO_x. This reagent-addition order can well control the solution pH; however, the employed MnO_x were mostly dry nanoparticles, which could undergo hydration and then homo-aggregation upon mixing in solution. If the reaction starts immediately after adding MnO_x, the MnO_x particles have not been well dispersed and hydrated, which might result in lower reactivity. To prove this point, we conducted one experiment, as the results shown in Fig. 11. Adding MnO_x and sonicating the solution for 5 min prior to Oxone addition enabled the observed reactivity to be higher than when MnO_x was added at last. Indeed, one typical practice in the studies that examined contaminant direct oxidation by MnO_x was to ensure that the MnO_x was well-hydrated before initiating the reaction (J. Huang et al., 2018; Taujale et al., 2016; Zhang and Huang, 2005; Zhang et al., 2015). Therefore, it is suggested that the MnO_x particles be well-hydrated prior to be engaged in catalytic reactions. Because oxide particles often undergo different degrees of aggregation depending on the surface charge (Taujale et al., 2016; Taujale and Zhang, 2012; Zhang et al., 2015), it might also be better to measure the particle sizes and surface areas in the aqueous phase if trying to correlate them with the catalytic reactivity.

8. Conclusions and future perspective

This review summarized the applications of Mn-based materials for the activation of PMS/PDS to remove contaminants in four aspects: (1) the different activation mechanisms of MnO_x, MnO_x hybrids and MnO_x-carbonaceous material hybrids, including free radical ($SO_4^{-\bullet}$ and $^{\bullet}OH$) and non-radical ($^1O_2$ and direct electron transfer) mechanisms, (2) the effects of solution pH, inorganic ions, NOM, temperature, and the crystallinity of Mn-based materials on the reactivity and mechanisms, (3) important methodologies and instruments to examine the reactions and materials, and (4) three overlooks in the experimental designs that might lead to errors in the observed reactivity. Although a number of articles have been published on the activation of PMS/PDS by Mn-based materials, there are still several challenges that need to be further investigated.

First, the amount of Mn(III) in Mn-based catalysts has been shown to be a key factor affecting the catalytic reactivity. Our recent work demonstrated that the mixed Mn valance (III/IV) of MnO_2 was important in its catalytic reactivity in PMS activation (Huang et al., 2019b), better than Mn(III) or Mn(IV) alone, which is similar to previous findings on MnO_2 as the catalysts for applications such as oxygen evolution reaction (Birkner et al., 2013; Indra et al., 2013; Kolling et al., 2012; Meng et al., 2014; Peng et al., 2017; Zaharieva et al., 2012). This might be related to the additional antibonding electron in Mn(III) that facilitates electron transfer between Mn(III) and Mn(IV) during the catalytic cycles (J. Huang et al., 2018). However, the optimum ratio of Mn(III)/Mn(IV) and the detailed mechanism for the activation of PMS/PDS need further study.

Second, not only the amount of Mn(III) in MnO_2 is affecting the reactivity, but different Mn(III) species in MnO_2 might have different catalytic reactivity. It has been shown that not all Mn(III) species are equally reactive, and a non-uniform distribution of Mn(III) perpendicular to the layer played an important role in the oxygen evolution reaction (Peng et al., 2017). Therefore, the difference in the Mn(III) contents and bonding environments in Mn_2O_3 and MnO_2 might have resulted in the different catalytic reactivity, which warrants further research.

Third, many doped MnO_x and their hybrids demonstrated better performance than pure MnO_x. It is important and necessary to understand what surface and structural properties are involved in the activation of PMS/PDS. The relationship between different physicochemical properties of these Mn-based catalysts and the catalytic reactivity should also be established, which will facilitate the comparison, design, and development of cost-effective catalysts for water/wastewater treatment.

Fourth, not much work has been done regarding employing Mn-based catalysts to activate PDS for the degradation of organic contaminants. It has been shown that the mechanisms of the activation of PDS and PMS by MnO_2 were different (Saputra et al., 2013c; Zhu et al., 2019). Given that PDS is an important oxidant for sulfate radicals-based advanced oxidation processes, it is necessary to investigate the mechanisms of PDS activation by Mn-based catalysts.

Fifth, although PMS/PDS has been employed for in situ chemical oxidation (ISCO) for decades in the remediation of contaminated soils (Do et al., 2010; Tsitonaki et al., 2010), little is known about how well Mn-based materials can activate PMS/PDS in these applications. It has been shown that MnO_x could enhance the performance of the PDS/Fe(II) system when treating a diesel-contaminated soil (Do et al., 2010), but the involved mechanism was not well understood. Therefore, it would be interesting to see if the knowledge gained from using Mn-based materials for water/wastewater treatment in the past few years can be applied to treat contaminated soil.

Finally, most of previous research examined MnO_x performance in batch experiments; thus, field applications of PMS/PDS-Mn-based materials should be further examined. For example, how do these materials respond to various water matrices at large scales? How can they be coated onto supports as the reactive media to remove contaminants? What are the potential application scenarios? After reaction for certain time, how can the spent materials be regenerated for extended usages? All this information will enable us to design cost-effective means to treat contaminants.

Acknowledgements

This research was financially supported by the U.S. National Science Foundation under Grants CBET-1762691 and CHE-1808406 to H. Zhang.

Declaration of competing interest

The authors declare that they have no known competing financial interests or personal relationships that could have appeared to influence the work reported in this paper.

References

Adjimi, S., García-Vargas, J., Díaz, J., Retailleau, L., Gil, S., Pera-Titus, M., Guo, Y., Giroir-

Fendler, A., 2017. Highly efficient and stable Ru/K-OMS-2 catalyst for NO oxidation. Appl. Catal., B 219, 459–466.

Afzal, M., Yu, M., Tang, C., Zhang, L., Muhammad, N., Zhao, H., Feng, J., Yu, L., Xu, J., 2019. The negative impact of cadmium on nitrogen transformation processes in a paddy soil is greater under non-flooding than flooding conditions. Environ. Int. 129, 451–460.

Agathokleous, E., Kitao, M., Calabrese, E.J., 2018. Human and veterinary antibiotics induce hormesis in plants: scientific and regulatory issues and an environmental perspective. Environ. Int. 120, 489–495.

Ahmad, M., Teel, A.L., Watts, R.J., 2010. Persulfate activation by subsurface minerals. J. Contam. Hydrol. 115 (1–4), 34–45.

Anipsitakis, G.P., Dionysiou, D.D., 2003. Degradation of organic contaminants in water with sulfate radicals generated by the conjunction of peroxymonosulfate with cobalt. Environ. Sci. Technol. 37 (20), 4790–4797.

Anipsitakis, G.P., Dionysiou, D.D., 2004a. Radical generation by the interaction of transition metals with common oxidants. Environ. Sci. Technol. 38 (13), 3705–3712.

Anipsitakis, G.P., Dionysiou, D.D., 2004b. Transition metal/UV-based advanced oxidation technologies for water decontamination. Appl. Catal., B 54 (3), 155–163.

Ao, X., Liu, W., 2017. Degradation of sulfamethoxazole by medium pressure UV and oxidants: peroxymonosulfate, persulfate, and hydrogen peroxide. Chem. Eng. J. 313, 629–637.

Atlas, R.M., 1981. Microbial degradation of petroleum hydrocarbons: an environmental perspective. Microbiol. Rev. 45 (1), 180.

Bagus, P.S., Broer, R., Ilton, E.S., 2004. A new near degeneracy effect for photoemission in transition metals. Chem. Phys. Lett. 394 (1–3), 150–154.

Bandara, J., Kiwi, J., 1999. Fast kinetic spectroscopy, decoloration and production of H_2O_2 induced by visible light in oxygenated solutions of the azo dye Orange II. New J. Chem. 23 (7), 717–724.

Béguin, P., Aubert, J.-P., 1994. The biological degradation of cellulose. FEMS Microbiol. Rev. 13 (1), 25–58.

Birkner, N., Nayeri, S., Pashaei, B., Najafpour, M.M., Casey, W.H., Navrotsky, A., 2013. Energetic basis of catalytic activity of layered nanophase calcium manganese oxides for water oxidation. PNAS 110 (22), 8801–8806.

Biswas, S., Poyraz, A.S., Meng, Y., Kuo, C.-H., Guild, C., Tripp, H., Suib, S.L., 2015. Ion induced promotion of activity enhancement of mesoporous manganese oxides for aerobic oxidation reactions. Appl. Catal., B 165, 731–741.

Brandt, C., Van Eldik, R., 1995. Transition metal-catalyzed oxidation of sulfur(IV) oxides. Atmospheric-relevant processes and mechanisms. Chem. Rev. 95 (1), 119–190.

Brock, S.L., Duan, N., Tian, Z.R., Giraldo, O., Zhou, H., Suib, S.L., 1998. A review of porous manganese oxide materials. Chem. Mater. 10 (10), 2619–2628.

Buxton, G.V., Greenstock, C.L., Helman, W.P., Ross, A.B., 1988. Critical review of rate constants for reactions of hydrated electrons, hydrogen atoms and hydroxyl radicals ($\cdot OH/\cdot O^-$) in aqueous solution. J. Phys. Chem. Ref. Data 17 (2), 513–886.

Caron-Beaudoin, É., Ayotte, P., Laouan Sidi, E.A., Gros-Louis McHugh, N., Lemire, M., 2019. Exposure to perfluoroalkyl substances (PFAS) and associations with thyroid parameters in first nation children and youth from Quebec. Environ. Int. 128, 13–23.

Cerrato, J.M., Hochella Jr., M.F., Knocke, W.R., Dietrich, A.M., Cromer, T.F., 2010. Use of XPS to identify the oxidation state of Mn in solid surfaces of filtration media oxide samples from drinking water treatment plants. Environ. Sci. Technol. 44 (15), 5881–5886.

Chen, C.-Y., Jafvert, C.T., 2010. Photoreactivity of carboxylated single-walled carbon nanotubes in sunlight: reactive oxygen species production in water. Environ. Sci. Technol. 44 (17), 6674–6679.

Chen, Y., Zhang, H., 2013. Complexation facilitated reduction of aromatic N-oxides by aqueous Fe^{II}–tiron complex: reaction kinetics and mechanisms. Environ. Sci. Technol. 47 (19), 11023–11031.

Chen, X., Wang, W., Xiao, H., Hong, C., Zhu, F., Yao, Y., Xue, Z., 2012. Accelerated TiO_2 photocatalytic degradation of Acid Orange 7 under visible light mediated by peroxymonosulfate. Chem. Eng. J. 193-194, 290–295.

Chen, Y., Dong, H., Zhang, H., 2016. Experimental and computational evidence for the reduction mechanisms of aromatic N-oxides by aqueous Fe^{II}–tiron complex. Environ. Sci. Technol. 50 (1), 249–258.

Chen, G., Zhang, X., Gao, Y., Zhu, G., Cheng, Q., Cheng, X., 2019. Novel magnetic MnO_2/$MnFe_2O_4$ nanocomposite as a heterogeneous catalyst for activation of peroxymonosulfate (PMS) toward oxidation of organic pollutants. Sep. Purif. Technol. 213, 456–464.

Criquet, J., Leitner, N.K.V., 2015. Reaction pathway of the degradation of the p-hydroxybenzoic acid by sulfate radical generated by ionizing radiations. Radiat. Phys. Chem. 106, 307–314.

Deng, J., Feng, S., Ma, X., Tan, C., Wang, H., Zhou, S., Zhang, T., Li, J., 2016. Heterogeneous degradation of Orange II with peroxymonosulfate activated by ordered mesoporous $MnFe_2O_4$. Sep. Purif. Technol. 167, 181–189.

Deng, J., Cheng, Y., Lu, Y., Crittenden, J.C., Zhou, S., Gao, N., Li, J., 2017a. Mesoporous manganese cobaltite nanocages as effective and reusable heterogeneous peroxymonosulfate activators for carbamazepine degradation. Chem. Eng. J. 330, 505–517.

Deng, J., Ge, Y., Tan, C., Wang, H., Li, Q., Zhou, S., Zhang, K., 2017b. Degradation of ciprofloxacin using α-MnO_2 activated peroxymonosulfate process: effect of water constituents, degradation intermediates and toxicity evaluation. Chem. Eng. J. 330, 1390–1400.

Devi, P., Das, U., Dalai, A.K., 2016. In-situ chemical oxidation: principle and applications of peroxide and persulfate treatments in wastewater systems. Sci. Total Environ. 571, 643–657.

Dickerson, A.S., Ransome, Y., Karlsson, O., 2019. Human prenatal exposure to polychlorinated biphenyls (PCBs) and risk behaviors in adolescence. Environ. Int. 129, 247–255.

Ding, Y., Zhu, L., Wang, N., Tang, H., 2013. Sulfate radicals induced degradation of tetrabromobisphenol A with nanoscaled magnetic $CuFe_2O_4$ as a heterogeneous catalyst of peroxymonosulfate. Appl. Catal., B 129, 153–162.

Ding, Y., Xia, X., Ruan, Y., Tang, H., 2015. In situ H^+-mediated formation of singlet oxygen from $NaBiO_3$ for oxidative degradation of bisphenol A without light irradiation: efficiency, kinetics, and mechanism. Chemosphere 141, 80–86.

Do, S.-H., Kwon, Y.-J., Kong, S.-H., 2010. Effect of metal oxides on the reactivity of persulfate/Fe(II) in the remediation of diesel-contaminated soil and sand. J. Hazard. Mater. 182 (1), 933–936.

Do, S.-H., Kwon, Y.-J., Bang, S.-J., Kong, S.-H., 2013. Persulfate reactivity enhanced by Fe_2O_3–MnO and CaO–Fe_2O_3–MnO composite: identification of composite and degradation of CCl_4 at various levels of pH. Chem. Eng. J. 221, 72–80.

Dong, Z., Zhang, Q., Chen, B.-Y., Hong, J., 2019. Oxidation of bisphenol A by persulfate via Fe_3O_4-α-MnO_2 nanoflower-like catalyst: mechanism and efficiency. Chem. Eng. J. 357, 337–347.

Du, J., Bao, J., Liu, Y., Ling, H., Zheng, H., Kim, S.H., Dionysiou, D.D., 2016. Efficient activation of peroxymonosulfate by magnetic Mn-MGO for degradation of bisphenol a. J. Hazard. Mater. 320 (Supplement C), 150–159.

Du, J., Bao, J., Liu, Y., Kim, S.H., Dionysiou, D.D., 2018. Facile preparation of porous Mn/Fe_3O_4 cubes as peroxymonosulfate activating catalyst for effective bisphenol A degradation. Chem. Eng. J. https://doi.org/10.1016/j.cej.2018.1005.1177.

Duan, X., Ao, Z., Sun, H., Indrawirawan, S., Wang, Y., Kang, J., Liang, F., Zhu, Z.H., Wang, S., 2015a. Nitrogen-doped graphene for generation and evolution of reactive radicals by metal-free catalysis. ACS Appl. Mater. Interfaces 7 (7), 4169–4178.

Duan, X., Indrawirawan, S., Sun, H., Wang, S., 2015b. Effects of nitrogen-, boron-, and phosphorus-doping or codoping on metal-free graphene catalysis. Catal. Today 249, 184–191.

Duan, X., Sun, H., Shao, Z., Wang, S., 2018a. Nonradical reactions in environmental remediation processes: uncertainty and challenges. Appl. Catal., B 224, 973–982.

Duan, X., Sun, H., Wang, S., 2018b. Metal-free carbocatalysis in advanced oxidation reactions. Acc. Chem. Res. 51 (3), 678–687.

Fan, J., Qin, H., Jiang, S., 2019. Mn-doped g-C_3N_4 composite to activate peroxymonosulfate for acetaminophen degradation: the role of superoxide anion and singlet oxygen. Chem. Eng. J. 359, 723–732.

Fang, G.-D., Dionysiou, D.D., Wang, Y., Al-Abed, S.R., Zhou, D.-M., 2012. Sulfate radical-based degradation of polychlorinated biphenyls: effects of chloride ion and reaction kinetics. J. Hazard. Mater. 227-228, 394–401.

Fang, G.-D., Dionysiou, D.D., Al-Abed, S.R., Zhou, D.-M., 2013. Superoxide radical driving the activation of persulfate by magnetite nanoparticles: implications for the degradation of PCBs. Appl. Catal., B 129, 325–332.

Fernández-Castro, P., Vallejo, M., San Román, M.F., Ortiz, I., 2015. Insight on the fundamentals of advanced oxidation processes. Role and review of the determination methods of reactive oxygen species. J. Chem. Technol. Biotechnol. 90 (5), 796–820.

Fontmorin, J., Castillo, R.B., Tang, W., Sillanpää, M., 2016. Stability of 5, 5-dimethyl-1-pyrroline-N-oxide as a spin-trap for quantification of hydroxyl radicals in processes based on Fenton reaction. Water Res. 99, 24–32.

Gao, P., Tian, X., Nie, Y., Yang, C., Zhou, Z., Wang, Y., 2019. Promoted peroxymonosulfate activation into singlet oxygen over perovskite for ofloxacin degradation by controlling the oxygen defect concentration. Chem. Eng. J. 359, 828–839.

Gao, Y.-q., Gao, N.-y., Chu, W.-h., Zhang, Y.-f., Zhang, J., Yin, D.-q., 2019. UV-activated persulfate oxidation of sulfamethoxypyridazine: kinetics, degradation pathways and impact on DBP formation during subsequent chlorination. Chem. Eng. J. 370, 706–715.

Ghanbari, F., Moradi, M., 2017. Application of peroxymonosulfate and its activation methods for degradation of environmental organic pollutants: review. Chem. Eng. J. 310 (Part 1), 41–62.

Gopi, T., Swetha, G., Chandra Shekar, S., Ramakrishna, C., Saini, B., Krishna, R., Rao, P.V.L., 2017. Catalytic decomposition of ozone on nanostructured potassium and proton containing δ-MnO_2 catalysts. Catal. Commun. 92, 51–55.

Guan, Y.-H., Ma, J., Ren, Y.-M., Liu, Y.-L., Xiao, J.-Y., Lin, L.-q., Zhang, C., 2013. Efficient degradation of atrazine by magnetic porous copper ferrite catalyzed peroxymonosulfate oxidation via the formation of hydroxyl and sulfate radicals. Water Res. 47 (14), 5431–5438.

Guo, Y., Zeng, Z., Zhu, Y., Huang, Z., Cui, Y., Yang, J., 2018. Catalytic oxidation of aqueous organic contaminants by persulfate activated with sulfur-doped hierarchically porous carbon derived from thiophene. Appl. Catal., B 220, 635–644.

Hao, S.M., Qu, J., Zhu, Z.S., Zhang, X.Y., Wang, Q.Q., Yu, Z.Z., 2016. Hollow manganese silicate nanotubes with tunable secondary nanostructures as excellent Fenton-type catalysts for dye decomposition at ambient temperature. Adv. Funct. Mater. 26 (40), 7334–7342.

Hao, S.-M., Yu, M.-Y., Zhang, Y.-J., Abdelkrim, Y., Qu, J., 2019. Hierarchical mesoporous cobalt silicate architectures as high-performance sulfate-radical-based advanced oxidization catalysts. J. Colloid Interface Sci. 545, 128–137.

Hermanek, M., Zboril, R., Medrik, I., Pechousek, J., Gregor, C., 2007. Catalytic efficiency of iron(III) oxides in decomposition of hydrogen peroxide: competition between the surface area and crystallinity of nanoparticles. JACS 129 (35), 10929–10936.

Hicks, M., Gebicki, J.M., 1986. Rate constants for reaction of hydroxyl radicals with Tris, Tricine and Hepes buffers. FEBS Lett. 199 (1), 92–94.

Hou, L., Li, X., Yang, Q., Chen, F., Wang, S., Ma, Y., Wu, Y., Zhu, X., Huang, X., Wang, D., 2019. Heterogeneous activation of peroxymonosulfate using Mn-Fe layered double hydroxide: performance and mechanism for organic pollutant degradation. Sci. Total Environ. 663, 453–464.

Hou, S., Zheng, N., Tang, L., Ji, X., Li, Y., Hua, X., 2019. Pollution characteristics, sources, and health risk assessment of human exposure to Cu, Zn, Cd and Pb pollution in urban street dust across China between 2009 and 2018. Environ. Int. 128, 430–437.

Houas, A., Lachheb, H., Ksibi, M., Elaloui, E., Guillard, C., Herrmann, J.-M., 2001.

Photocatalytic degradation pathway of methylene blue in water. Appl. Catal., B 31 (2), 145–157.

Hu, P., Long, M., 2016. Cobalt-catalyzed sulfate radical-based advanced oxidation: a review on heterogeneous catalysts and applications. Appl. Catal., B 181, 103–117.

Hu, J., Dong, H., Qu, J., Qiang, Z., 2017. Enhanced degradation of iopamidol by peroxymonosulfate catalyzed by two pipe corrosion products (CuO and δ-MnO_2). Water Res. 112, 1–8.

Hu, L., Deng, G., Lu, W., Lu, Y., Zhang, Y., 2017. Peroxymonosulfate activation by Mn_3O_4/metal-organic framework for degradation of refractory aqueous organic pollutant rhodamine B. Chin. J. Catal. 38 (8), 1360–1372.

Hu, P., Su, H., Chen, Z., Yu, C., Li, Q., Zhou, B., Alvarez, P.J.J., Long, M., 2017. Selective degradation of organic pollutants using an efficient metal-free catalyst derived from carbonized polypyrrole via peroxymonosulfate activation. Environ. Sci. Technol. 51 (19), 11288–11296.

Huang, G.-X., Wang, C.-Y., Yang, C.-W., Guo, P.-C., Yu, H.-Q., 2017. Degradation of bisphenol A by peroxymonosulfate catalytically activated with $Mn_{1.8}Fe_{1.2}O_4$ nanospheres: synergism between Mn and Fe. Environ. Sci. Technol. 51 (21), 12611–12618.

Huang, J., Zhong, S., Dai, Y., Liu, C.-C., Zhang, H., 2018. Effect of MnO_2 phase structure on the oxidative reactivity toward bisphenol A degradation. Environ. Sci. Technol. 52 (19), 11309–11318.

Huang, Y., Tian, X., Nie, Y., Yang, C., Wang, Y., 2018. Enhanced peroxymonosulfate activation for phenol degradation over MnO_2 at pH 3.5–9.0 via Cu(II) substitution. J. Hazard. Mater. 360, 303–310.

Huang, J., Dai, Y., Liu, C.-C., Zhang, H., 2019a. Effects of second metal oxides on surface-mediated reduction of contaminants by Fe(II) with iron oxide. ACS Earth Space Chem. 3 (5), 680–687.

Huang, J., Dai, Y., Singewald, K., Liu, C.-C., Saxena, S., Zhang, H., 2019b. Effects of MnO_2 of different structures on activation of peroxymonosulfate for bisphenol A degradation under acidic conditions. Chem. Eng. J. 370, 906–915.

Huang, J., Wang, Q., Wang, Z., Zhang, H.J., 2019c. Interactions and reductive reactivity in ternary mixtures of Fe(II), goethite, and phthalic acid based on a combined experimental and modeling approach. Langmuir 35, 8220–8227.

Ike, I.A., Linden, K.G., Orbell, J.D., Duke, M., 2018. Critical review of the science and sustainability of persulphate advanced oxidation processes. Chem. Eng. J. 338, 651–669.

Ilton, E.S., Post, J.E., Heaney, P.J., Ling, F.T., Kerisit, S.N., 2016. XPS determination of Mn oxidation states in Mn (hydr)oxides. Appl. Sci. Res. 366 (Supplement C), 475–485.

Indra, A., Menezes, P.W., Zaharieva, I., Baktash, E., Pfrommer, J., Schwarze, M., Dau, H., Driess, M., 2013. Active mixed-valent MnO_x water oxidation catalysts through partial oxidation (corrosion) of nanostructured MnO particles. Angew. Chem. 52 (50), 13206–13210.

Islam, M.A., Morton, D.W., Johnson, B.B., Mainali, B., Angove, M.J., 2018. Manganese oxides and their application to metal ion and contaminant removal from wastewater. J. Water Proc. Eng. 26, 264–280.

Jadbabaei, N., Ye, T., Shuai, D., Zhang, H., 2017. Development of palladium-resin composites for catalytic hydrodechlorination of 4-chlorophenol. Appl. Catal., B 205, 576–586.

Jiang, Z., Yang, H., Wei, Z., Xie, Z., Zhong, W., Wei, S., 2005. Catalytic properties and structures of nano-amorphous Ni–B alloys affected by annealing temperatures. Appl. Catal., A 279 (1–2), 165–171.

Jiang, M., Lu, J., Ji, Y., Kong, D., 2017. Bicarbonate-activated persulfate oxidation of acetaminophen. Water Res. 116, 324–331.

Jo, Y.-H., Do, S.-H., Kong, S.-H., 2014a. Persulfate activation by iron oxide-immobilized MnO_2 composite: identification of iron oxide and the optimum pH for degradations. Chemosphere 95, 550–555.

Jo, Y.-H., Hong, S.-H., Park, T.-J., Do, S.-H., 2014b. The synthesized and thermally modified Mn–Ca–FeOOH composite in persulfate system: its role to discolor methylene blue. Appl. Sci. Res. 301, 576–583.

Khan, A., Liao, Z., Liu, Y., Jawad, A., Ifthikar, J., Chen, Z., 2017. Synergistic degradation of phenols using peroxymonosulfate activated by CuO-Co_3O_4@MnO_2 nanocatalyst. J. Hazard. Mater. 329, 262–271.

Khan, A., Wang, H., Liu, Y., Jawad, A., Ifthikar, J., Liao, Z., Wang, T., Chen, Z., 2018a. Highly efficient α-Mn_2O_3@α-MnO_2-500 nanocomposite for peroxymonosulfate activation: comprehensive investigation of manganese oxides. J. Mater. Chem. A 6, 1590–1600.

Khan, A., Zou, S., Wang, T., Ifthikar, J., Jawad, A., Liao, Z., Shahzad, A., Ngambia, A., Chen, Z., 2018b. Facile synthesis of yolk shell Mn_2O_3@Mn_5O_8 as an effective catalyst for peroxymonosulfate activation. Phys. Chem. Chem. Phys. 20 (20), 13909–13919.

Kim, E.-J., Oh, D., Lee, C.-S., Gong, J., Kim, J., Chang, Y.-S., 2016. Manganese oxide nanorods as a robust Fenton-like catalyst at neutral pH: crystal phase-dependent behavior. Catal. Today 282, 71–76.

King'ondu, C.K., Opembe, N., Chen, C.h., Ngala, K., Huang, H., Iyer, A., Garces, H.F., Suib, S.L., 2011. Manganese oxide octahedral molecular sieves (OMS-2) multiple framework substitutions: a new route to OMS-2 particle size and morphology control. Adv. Funct. Mater. 21 (2), 312–323.

Kolling, D.R., Cox, N., Ananyev, G.M., Pace, R.J., Dismukes, G.C., 2012. What are the oxidation states of manganese required to catalyze photosynthetic water oxidation? Biophys. J. 103 (2), 313–322.

Li, W., Wu, P.-x., Zhu, Y., Huang, Z.-j., Lu, Y.-h., Li, Y.-w., Dang, Z., Zhu, N.-w., 2015. Catalytic degradation of bisphenol A by CoMnAl mixed metal oxides catalyzed peroxymonosulfate: performance and mechanism. Chem. Eng. J. 279, 93–102.

Li, Y., Liu, L.-D., Liu, L., Liu, Y., Zhang, H.-W., Han, X., 2016. Efficient oxidation of phenol by persulfate using manganite as a catalyst. J. Mol. Catal. A Chem. 411, 264–271.

Li, J., Fang, J., Gao, L., Zhang, J., Ruan, X., Xu, A., Li, X., 2017a. Graphitic carbon nitride induced activity enhancement of OMS-2 catalyst for pollutants degradation with peroxymonosulfate. Appl. Sci. Res. 402, 352–359.

Li, J., Ye, P., Fang, J., Wang, M., Wu, D., Xu, A., Li, X., 2017b. Peroxymonosulfate activation and pollutants degradation over highly dispersed CuO in manganese oxide octahedral molecular sieve. Appl. Sci. Res. 422, 754–762.

Li, C., Wu, J., Peng, W., Fang, Z., Liu, J., 2019. Peroxymonosulfate activation for efficient sulfamethoxazole degradation by Fe_3O_4/β-FeOOH nanocomposites: coexistence of radical and non-radical reactions. Chem. Eng. J. 356, 904–914.

Liang, C., Wang, Z.-S., Mohanty, N., 2006. Influences of carbonate and chloride ions on persulfate oxidation of trichloroethylene at 20 °C. Sci. Total Environ. 370 (2–3), 271–277.

Liang, H., Sun, H., Patel, A., Shukla, P., Zhu, Z., Wang, S., 2012. Excellent performance of mesoporous Co_3O_4/MnO_2 nanoparticles in heterogeneous activation of peroxymonosulfate for phenol degradation in aqueous solutions. Appl. Catal., B 127, 330–335.

Liang, H., Meng, F., Cabán-Acevedo, M., Li, L., Forticaux, A., Xiu, L., Wang, Z., Jin, S., 2015. Hydrothermal continuous flow synthesis and exfoliation of NiCo layered double hydroxide nanosheets for enhanced oxygen evolution catalysis. Nano Lett. 15 (2), 1421–1427.

Lin, H., Li, S., Deng, B., Tan, W., Li, R., Xu, Y., Zhang, H., 2019. Degradation of bisphenol A by activating peroxymonosulfate with $Mn_{0.6}Zn_{0.4}Fe_2O_4$ fabricated from spent Zn-Mn alkaline batteries. Chem. Eng. J. 364, 541–551.

Lin, Y.-Z., Zhong, L.-B., Dou, S., Shao, Z.-D., Liu, Q., Zheng, Y.-M., 2019. Facile synthesis of electrospun carbon nanofiber/graphene oxide composite aerogels for high efficiency oils absorption. Environ. Int. 128, 37–45.

Liu, J., Zhao, Z., Shao, P., Cui, F., 2015. Activation of peroxymonosulfate with magnetic Fe_3O_4–MnO_2 core–shell nanocomposites for 4-chlorophenol degradation. Chem. Eng. J. 262, 854–861.

Liu, C., Pan, D., Tang, X., Hou, M., Zhou, Q., Zhou, J., 2016. Degradation of Rhodamine B by the α-MnO_2/peroxymonosulfate system. Water Air Soil Pollut. 227 (3), 92.

Liu, Q., Duan, X., Sun, H., Wang, Y., Tade, M.O., Wang, S., 2016. Size-tailored porous spheres of manganese oxides for catalytic oxidation via peroxymonosulfate activation. J. Phys. Chem. C 120 (30), 16871–16878.

Liu, C., Wu, B., Chen, X.e., 2018. Sulfate radical-based oxidation for sludge treatment: a review. Chem. Eng. J. 335, 865–875.

Liu, J., Wang, J., Ning, Y., Yang, S., Wang, P., Shaheen, S.M., Feng, X., Rinklebe, J., 2019. Methylmercury production in a paddy soil and its uptake by rice plants as affected by different geochemical mercury pools. Environ. Int. 129, 461–469.

Lu, X., Zhai, T., Zhang, X., Shen, Y., Yuan, L., Hu, B., Gong, L., Chen, J., Gao, Y., Zhou, J., 2012. WO_{3-x}@Au@ MnO_2 core–shell nanowires on carbon fabric for high-performance flexible supercapacitors. Adv. Mater. 24 (7), 938–944.

Luo, S., Duan, L., Sun, B., Wei, M., Li, X., Xu, A., 2015. Manganese oxide octahedral molecular sieve (OMS-2) as an effective catalyst for degradation of organic dyes in aqueous solutions in the presence of peroxymonosulfate. Appl. Catal., B 164, 92–99.

Luo, X., Liang, H., Qu, F., Ding, A., Cheng, X., Tang, C.Y., Li, G., 2018. Free-standing hierarchical α-MnO_2@CuO membrane for catalytic filtration degradation of organic pollutants. Chemosphere 200, 237–247.

Luo, H., Xie, Y., Niu, J., Xiao, Y., Li, Y., Wang, Y., Zhang, Y., Xie, T., 2019. Cobalt-doped biogenic manganese oxides for enhanced tetracycline degradation by activation of peroxymonosulfate. J. Chem. Technol. Biotechnol. 94 (3), 752–760.

Ma, Q., Zhang, H., Zhang, X., Li, B., Guo, R., Cheng, Q., Cheng, X., 2019a. Synthesis of magnetic CuO/$MnFe_2O_4$ nanocompisite and its high activity for degradation of levofloxacin by activation of persulfate. Chem. Eng. J. 360, 848–860.

Ma, Q., Zhang, X., Guo, R., Zhang, H., Cheng, Q., Xie, M., Cheng, X., 2019b. Persulfate activation by magnetic γ-Fe_2O_3/Mn_3O_4 nanocomposites for degradation of organic pollutants. Sep. Purif. Technol. 210, 335–342.

Mady, A.H., Baynosa, M.L., Tuma, D., Shim, J.-J., 2019. Heterogeneous activation of peroxymonosulfate by a novel magnetic 3D γ-MnO_2@$ZnFe_2O_4$/rGO nanohybrid as a robust catalyst for phenol degradation. Appl. Catal., B 244, 946–956.

Maeno, S., Zhu, Q., Sasaki, M., Miyamoto, T., Fukushima, M., 2015. Monopersulfate oxidation of tetrabromobisphenol A by an iron(III)-phthalocyaninetetrasulfate catalyst coordinated to imidazole functionalized silica particles. J. Mol. Catal. A Chem. 400, 56–63.

Maruthamuthu, P., Neta, P., 1978. Phosphate radicals. Spectra, acid-base equilibriums, and reactions with inorganic compounds. J. Phys. Chem. 82 (6), 710–713.

Matzek, L.W., Carter, K.E., 2016. Activated persulfate for organic chemical degradation: a review. Chemosphere 151, 178–188.

Meng, Y., Song, W., Huang, H., Ren, Z., Chen, S.-Y., Suib, S.L., 2014. Structure–property relationship of bifunctional MnO_2 nanostructures: highly efficient, ultra-stable electrochemical water oxidation and oxygen reduction reaction catalysts identified in alkaline media. JACS 136 (32), 11452–11464.

Merkel, P.B., Nilsson, R., Kearns, D.R., 1972. Deuterium effects on singlet oxygen lifetimes in solutions. A new test of singlet oxygen reactions. JACS 94 (3), 1030–1031.

Miao, J., Sunarso, J., Duan, X., Zhou, W., Wang, S., Shao, Z., 2018. Nanostructured Co-Mn containing perovskites for degradation of pollutants: insight into the activity and stability. J. Hazard. Mater. 349, 177–185.

Miao, J., Duan, X., Li, J., Dai, J., Liu, B., Wang, S., Zhou, W., Shao, Z., 2019. Boosting performance of lanthanide magnetism perovskite for advanced oxidation through lattice doping with catalytically inert element. Chem. Eng. J. 355, 721–730.

Nardi, G., Manet, I., Monti, S., Miranda, M.A., Lhiaubet-Vallet, V., 2014. Scope and limitations of the TEMPO/EPR method for singlet oxygen detection: the misleading role of electron transfer. Free Radic. Biol. Med. 77, 64–70.

Nau, W.M., Scaiano, J.C., 1996. Oxygen quenching of excited aliphatic ketones and diketones. J. Phys. Chem. 100 (27), 11360–11367.

Nicolaides, C., Sincadu, N., Scurrell, M., 2002. NAS (novel aluminosilicates) as catalysts for the aromatisation of propane: studies of zinc and gallium modified zeolite-based systems having various extents of XRD crystallinity. Catal. Today 71 (3–4), 429–435.

Nidheesh, P.V., Gandhimathi, R., Ramesh, S.T., 2013. Degradation of dyes from aqueous solution by Fenton processes: a review. Environ. Sci. Pollut. Res. Int. 20 (4), 2099–2132.

Nosaka, Y., Nosaka, A.Y., 2017. Generation and detection of reactive oxygen species in photocatalysis. Chem. Rev. 117 (17), 11302–11336.

Oh, W.-D., Lim, T.-T., 2019. Design and application of heterogeneous catalysts as peroxydisulfate activator for organics removal: an overview. Chem. Eng. J. 358, 110–133.

Oh, W.-D., Dong, Z., Lim, T.-T., 2016. Generation of sulfate radical through heterogeneous catalysis for organic contaminants removal: current development, challenges and prospects. Appl. Catal., B 194 (Supplement C), 169–201.

Pan, B., Zhang, H., 2012. A modified polanyi-based model for mechanistic understanding of adsorption of phenolic compounds onto polymeric adsorbents. Environ. Sci. Technol. 46 (12), 6806–6814.

Pan, Y., Su, H., Zhu, Y., Vafaei Molamahmood, H., Long, M., 2018. CaO_2 based Fenton-like reaction at neutral pH: accelerated reduction of ferric species and production of superoxide radicals. Water Res. 145, 731–740.

Pang, Y., Lei, H., 2016. Degradation of p-nitrophenol through microwave-assisted heterogeneous activation of peroxymonosulfate by manganese ferrite. Chem. Eng. J. 287, 585–592.

Peluso, M.A., Gambaro, L.A., Pronsato, E., Gazzoli, D., Thomas, H.J., Sambeth, J.E., 2008. Synthesis and catalytic activity of manganese dioxide (type OMS-2) for the abatement of oxygenated VOCs. Catal. Today 133-135, 487–492.

Peng, W.-c., Wang, S.-b., Li, X.-y., 2016. Shape-controlled synthesis of one-dimensional α-MnO_2 nanocrystals for organic detection and pollutant degradation. Sep. Purif. Technol. 163, 15–22.

Peng, H., McKendry, I.G., Ding, R., Thenuwara, A.C., Kang, Q., Shumlas, S.L., Strongin, D.R., Zdilla, M.J., Perdew, J.P., 2017. Redox properties of birnessite from a defect perspective. PNAS 114 (36), 9523–9528.

Pollack, A.Z., Mumford, S.L., Krall, J.R., Carmichael, A.E., Sjaarda, L.A., Perkins, N.J., Kannan, K., Schisterman, E.F., 2018. Exposure to bisphenol a, chlorophenols, benzophenones, and parabens in relation to reproductive hormones in healthy women: a chemical mixture approach. Environ. Int. 120, 137–144.

Qu, S., Li, C., Sun, X., Wang, J., Luo, H., Wang, S., Ta, J., Li, D., 2019. Enhancement of peroxymonosulfate activation and utilization efficiency via iron oxychloride nanosheets in visible light. Sep. Purif. Technol. 224, 132–141.

Raman, L.P., Cheryna, M., Rajagopalan, N., 1994. Consider nanofiltration for membrane separations. Chem. Eng. Prog. 90 (3).

Remucal, C.K., Ginder-Vogel, M., 2014. A critical review of the reactivity of manganese oxides with organic contaminants. Environ. Sci.: Processes Impacts 16 (6), 1247–1266.

Ren, Y., Lin, L., Ma, J., Yang, J., Feng, J., Fan, Z., 2015. Sulfate radicals induced from peroxymonosulfate by magnetic ferrospinel MFe_2O_4 (M = Co, Cu, Mn, and Zn) as heterogeneous catalysts in the water. Appl. Catal., B 165, 572–578.

Rosen, G.M., Rauckman, E.J., 1980. Spin trapping of the primary radical involved in the activation of the carcinogen N-hydroxy-2-acetylaminofluorene by cumene hydroperoxide-hematin. Mol. Pharmacol. 17 (2), 233–238.

Sabri, M., King, H.J., Gummow, R.J., Lu, X., Zhao, C., Oelgemöller, M., Chang, S.L., Hocking, R.K., 2018. Oxidant or catalyst for oxidation? A study of how structure and disorder change the selectivity for direct versus catalytic oxidation mediated by manganese (III, IV) oxides. Chem. Mater. 30 (22), 8244–8256.

Saputra, E., Muhammad, S., Sun, H., Patel, A., Shukla, P., Zhu, Z., Wang, S., 2012. α-MnO_2 activation of peroxymonosulfate for catalytic phenol degradation in aqueous solutions. Catal. Commun. 26, 144–148.

Saputra, E., Muhammad, S., Sun, H., Ang, H.-M., Tadé, M.O., Wang, S., 2013a. A comparative study of spinel structured Mn_3O_4, Co_3O_4 and Fe_3O_4 nanoparticles in catalytic oxidation of phenolic contaminants in aqueous solutions. J. Colloid Interface Sci. 407, 467–473.

Saputra, E., Muhammad, S., Sun, H., Ang, H.-M., Tadé, M.O., Wang, S., 2013b. Manganese oxides at different oxidation states for heterogeneous activation of peroxymonosulfate for phenol degradation in aqueous solutions. Appl. Catal., B 142, 729–735.

Saputra, E., Muhammad, S., Sun, H., Ang, H.M., Tade, M., Wang, S., 2013c. Different crystallographic one-dimensional MnO_2 nanomaterials and their superior performance in catalytic phenol degradation. Environ. Sci. Technol. 47 (11), 5882–5887.

Saputra, E., Muhammad, S., Sun, H., Ang, H.-M., Tadé, M.O., Wang, S., 2014a. Shape-controlled activation of peroxymonosulfate by single crystal α-Mn_2O_3 for catalytic phenol degradation in aqueous solution. Appl. Catal., B 154, 246–251.

Saputra, E., Muhammad, S., Sun, H., Ang, H.-M., Tadé, M.O., Wang, S., 2014b. β-MnO_2 activation of peroxymonosulfate for catalytic phenol degradation in aqueous solutions. CHEMICA Jurnal Teknik Kimia 1 (1), 19–26.

Saputra, E., Zhang, H., Liu, Q., Sun, H., Wang, S., 2016. Egg-shaped core/shell α-Mn_2O_3@α-MnO_2 as heterogeneous catalysts for decomposition of phenolics in aqueous solutions. Chemosphere 159, 351–358.

Selvakumar, S., Nuns, N., Trentesaux, M., Batra, V.S., Giraudon, J.M., Lamonier, J.F., 2018. Reaction of formaldehyde over birnessite catalyst: a combined XPS and ToF-SIMS study. Appl. Catal., B 223, 192–200.

Shah, N.S., He, X., Khan, H.M., Khan, J.A., O'Shea, K.E., Boccelli, D.L., Dionysiou, D.D., 2013. Efficient removal of endosulfan from aqueous solution by UV-C/peroxides: a comparative study. J. Hazard. Mater. 263, 584–592.

Shah, N.S., Ali Khan, J., Sayed, M., Ul Haq Khan, Z., Sajid Ali, H., Murtaza, B., Khan, H.M., Imran, M., Muhammad, N., 2019. Hydroxyl and sulfate radical mediated degradation of ciprofloxacin using nano zerovalent manganese catalyzed $S_2O_8^{2-}$. Chem. Eng. J. 356, 199–209.

Shaikh N., Taujale, Saru, Zhang H., K. Artyushkova A.-M.S.A., Cerrato J.M., 2016. Spectroscopic investigation of interfacial interaction of manganese oxide with triclosan, aniline, and phenol. Environ. Sci. Technol. 50 (20), 10978–10987.

Sirés, I., Brillas, E., Oturan, M.A., Rodrigo, M.A., Panizza, M., 2014. Electrochemical advanced oxidation processes: today and tomorrow. A review. Environ. Sci. Pollut. Res. Int. 21 (14), 8336–8367.

Smith, B.A., Teel, A.L., Watts, R.J., 2006. Mechanism for the destruction of carbon tetrachloride and chloroform DNAPLs by modified Fenton's reagent. J. Contam. Hydrol. 85 (3), 229–246.

Stasinakis, A., 2008. Use of selected advanced oxidation processes (AOPs) for wastewater treatment–a mini review. Global NEST J. 10 (3), 376–385.

Stone, A.T., 1987. Reductive dissolution of manganese (III/IV) oxides by substituted phenols. Environ. Sci. Technol. 21 (10), 979–988.

Sun, H., Wang, S., 2015. Catalytic oxidation of organic pollutants in aqueous solution using sulfate radicals. Catalysis 27, 209–247.

Sun, M., Lan, B., Lin, T., Cheng, G., Ye, F., Yu, L., Cheng, X., Zheng, X., 2013. Controlled synthesis of nanostructured manganese oxide: crystalline evolution and catalytic activities. CrystEngComm 15 (35), 7010–7018.

Tan, C., Gao, N., Deng, Y., An, N., Deng, J., 2012. Heat-activated persulfate oxidation of diuron in water. Chem. Eng. J. 203, 294–300.

Tang, D., Zhang, G., Guo, S., 2015. Efficient activation of peroxymonosulfate by manganese oxide for the degradation of azo dye at ambient condition. J. Colloid Interface Sci. 454, 44–51.

Tang, X., Huang, J., Liu, K., Feng, Q., Li, Z., Ao, M., 2018. Synthesis of magnetically separable MnO_2/Fe_3O_4/silica nanofiber composite with enhanced Fenton-like catalytic activity for degradation of acid red 73. Surf. Coat. Technol. 354, 18–27.

Taujale, S., Zhang, H., 2012. Impact of interactions between metal oxides to oxidative reactivity of manganese dioxide. Environ. Sci. Technol. 46 (5), 2764–2771.

Taujale, S., Baratta, L.R., Huang, J., Zhang, H., 2016. Interactions in ternary mixtures of MnO_2, Al_2O_3, and natural organic matter (NOM) and the impact on MnO_2 oxidative reactivity. Environ. Sci. Technol. 50 (5), 2345–2353.

Tian, S., Jiang, P., Ning, P., Su, Y., 2009. Enhanced adsorption removal of phosphate from water by mixed lanthanum/aluminum pillared montmorillonite. Chem. Eng. J. 151 (1), 141–148.

Tian, X., Gao, P., Nie, Y., Yang, C., Zhou, Z., Li, Y., Wang, Y., 2017. A novel singlet oxygen involved peroxymonosulfate activation mechanism for degradation of ofloxacin and phenol in water. Chem. Commun. 53 (49), 6589–6592.

Tian, N., Tian, X., Nie, Y., Yang, C., Zhou, Z., Li, Y., 2018. Biogenic manganese oxide: An efficient peroxymonosulfate activation catalyst for tetracycline and phenol degradation in water. Chem. Eng. J. 352, 469–476.

Tian, N., Tian, X., Nie, Y., Yang, C., Zhou, Z., Li, Y., 2019. Enhanced 2, 4-dichlorophenol degradation at pH 3–11 by peroxymonosulfate via controlling the reactive oxygen species over Ce substituted 3D Mn_2O_3. Chem. Eng. J. 355, 448–456.

Truong, T.T., Liu, Y., Ren, Y., Trahey, L., Sun, Y., 2012. Morphological and crystalline evolution of nanostructured MnO_2 and its application in lithium–air batteries. ACS Nano 6 (9), 8067–8077.

Tsitonaki, A., Petri, B., Crimi, M., Mosbæk, H., Siegrist, R.L., Bjerg, P.L., 2010. In situ chemical oxidation of contaminated soil and groundwater using persulfate: a review. Crit. Rev. Environ. Sci. Technol. 40 (1), 55–91.

Turchi, C.S., Ollis, D.F., 1990. Photocatalytic degradation of organic water contaminants: mechanisms involving hydroxyl radical attack. J. Catal. 122 (1), 178–192.

van Veldhoven, K., Keski-Rahkonen, P., Barupal, D.K., Villanueva, C.M., Font-Ribera, L., Scalbert, A., Bodinier, B., Grimalt, J.O., Zwiener, C., Vlaanderen, J., Portengen, L., Vermeulen, R., Vineis, P., Chadeau-Hyam, M., Kogevinas, M., 2018. Effects of exposure to water disinfection by-products in a swimming pool: a metabolome-wide association study. Environ. Int. 111, 60–70.

Vikesland, P.J., Heathcock, A.M., Rebodos, R.L., Makus, K.E., 2007. Particle size and aggregation effects on magnetite reactivity toward carbon tetrachloride. Environ. Sci. Technol. 41 (15), 5277–5283.

Wacławek, S., Lutze, H.V., Grübel, K., Padil, V.V.T., Černík, M., Dionysiou, D.D., 2017. Chemistry of persulfates in water and wastewater treatment: a review. Chem. Eng. J. 330, 44–62.

Waldemer, R.H., Tratnyek, P.G., Johnson, R.L., Nurmi, J.T., 2007. Oxidation of chlorinated ethenes by heat-activated persulfate: kinetics and products. Environ. Sci. Technol. 41 (3), 1010–1015.

Wan, J., Zhou, L., Deng, H., Zhan, F., Zhang, R., 2015. Oxidative degradation of sulfamethoxazole by different MnO_2 nanocrystals in aqueous solution. J. Mol. Catal. A Chem. 407, 67–74.

Wang, J., Chu, L., 2016. Biological nitrate removal from water and wastewater by solid-phase denitrification process. Biotechnol. Adv. 34 (6), 1103–1112.

Wang, J., Wang, S., 2018. Activation of persulfate (PS) and peroxymonosulfate (PMS) and application for the degradation of emerging contaminants. Chem. Eng. J. 334, 1502–1517.

Wang, Y., Sun, H., Ang, H.M., Tadé, M.O., Wang, S., 2014a. Synthesis of magnetic core/shell carbon nanosphere supported manganese catalysts for oxidation of organics in water by peroxymonosulfate. J. Colloid Interface Sci. 433, 68–75.

Wang, Y., Sun, H., Ang, H.M., Tadé, M.O., Wang, S., 2014b. Facile synthesis of hierarchically structured magnetic MnO_2/$ZnFe_2O_4$ hybrid materials and their performance in heterogeneous activation of peroxymonosulfate. ACS Appl. Mater. Interfaces 6 (22), 19914–19923.

Wang, S., Zhou, N., Wu, S., Zhang, Q., Yang, Z., 2015. Modeling the oxidation kinetics of sono-activated persulfate's process on the degradation of humic acid. Ultrason. Sonochem. 23, 128–134.

Wang, Y., Indrawirawan, S., Duan, X., Sun, H., Ang, H.M., Tadé, M.O., Wang, S., 2015a. New insights into heterogeneous generation and evolution processes of sulfate radicals for phenol degradation over one-dimensional α-MnO_2 nanostructures. Chem. Eng. J. 266, 12–20.

Wang, Y., Sun, H., Ang, H.M., Tadé, M.O., Wang, S., 2015b. 3D-hierarchically structured

MnO_2 for catalytic oxidation of phenol solutions by activation of peroxymonosulfate: structure dependence and mechanism. Appl. Catal., B 164 (0), 159–167.

Wang, L., Jiang, J., Pang, S.-Y., Zhou, Y., Li, J., Sun, S., Gao, Y., Jiang, C., 2018. Oxidation of bisphenol A by nonradical activation of peroxymonosulfate in the presence of amorphous manganese dioxide. Chem. Eng. J. 352, 1004–1013.

Wang, M., Wei, Y., Zou, Q., Zhang, W., Xu, A., Li, X., 2019. Tuning manganese (III) species in manganese oxide octahedral molecular sieve by interaction with carbon nanofibers for enhanced pollutant degradation in the presence of peroxymonosulfate. J. Colloid Interface Sci. 536, 271–280.

Wei, M., Ruan, Y., Luo, S., Li, X., Xu, A., Zhang, P., 2015. The facile synthesis of a magnetic OMS-2 catalyst for decomposition of organic dyes in aqueous solution with peroxymonosulfate. New J. Chem. 39 (8), 6395–6403.

Xiao, R., Luo, Z., Wei, Z., Luo, S., Spinney, R., Yang, W., Dionysiou, D.D., 2018. Activation of peroxymonosulfate/persulfate by nanomaterials for sulfate radical-based advanced oxidation technologies. Curr. Opin. Chem. Eng. 19, 51–58.

Xie, J., Wei, Y., Song, X., Chen, Y., Zou, Q., Wang, M., Xu, A., Li, X., 2018. Controlled growth of γ-MnO_2 nanoflakes on OMS-2 for efficient decomposition of organic dyes in aqueous solution via peroxymonosulfate activation. J. Colloid Interface Sci. 529, 476–482.

Xie, M., Tang, J., Kong, L., Lu, W., Natarajan, V., Zhu, F., Zhan, J., 2018. Cobalt doped g-C_3N_4 activation of peroxymonosulfate for monochlorophenols degradation. Chem. Eng. J. 360, 1213–1222.

Xie, X., Li, Y., Yang, Y., Chen, C., Zhang, Q., 2018. UV–vis–IR driven thermocatalytic activity of OMS-2/SnO_2 nanocomposite significantly enhanced by novel photo-activation and synergetic photocatalysis-thermocatalysis. Appl. Sci. Res. 462, 590–597.

Xie, Y., Li, P., Zeng, Y., Li, X., Xiao, Y., Wang, Y., Zhang, Y., 2018. Thermally treated fungal manganese oxides for bisphenol A degradation using sulfate radicals. Chem. Eng. J. 335, 728–736.

Xu, Y., Lin, H., Li, Y., Zhang, H., 2017. The mechanism and efficiency of MnO_2 activated persulfate process coupled with electrolysis. Sci. Total Environ. 609, 644–654.

Yang, J.-C.E., Lan, H., Lin, X.-Q., Yuan, B., Fu, M.-L., 2016. Synthetic conditions-regulated catalytic Oxone efficacy of MnO_x/SBA-15 towards butyl paraben (BPB) removal under heterogeneous conditions. Chem. Eng. J. 289, 296–305.

Yang, J.-C.E., Yuan, B., Cui, H.-J., Wang, S., Fu, M.-L., 2017. Modulating oxone-MnO_x/silica catalytic systems towards ibuprofen degradation: insights into system effects, reaction kinetics and mechanisms. Appl. Catal., B 205, 327–339.

Yang, Q., Yang, X., Yan, Y., Sun, C., Wu, H., He, J., Wang, D., 2018. Heterogeneous activation of peroxymonosulfate by different ferromanganese oxides for tetracycline degradation: structure dependence and catalytic mechanism. Chem. Eng. J. 348, 263–270.

Yao, Y., Xu, C., Yu, S., Zhang, D., Wang, S., 2013. Facile synthesis of Mn_3O_4–reduced graphene oxide hybrids for catalytic decomposition of aqueous organics. Ind. Eng. Chem. Res. 52 (10), 3637–3645.

Yao, Y., Cai, Y., Lu, F., Wei, F., Wang, X., Wang, S., 2014. Magnetic recoverable $MnFe_2O_4$ and $MnFe_2O_4$-graphene hybrid as heterogeneous catalysts of peroxymonosulfate activation for efficient degradation of aqueous organic pollutants. J. Hazard. Mater. 270, 61–70.

Yao, Y., Cai, Y., Wu, G., Wei, F., Li, X., Chen, H., Wang, S., 2015. Sulfate radicals induced from peroxymonosulfate by cobalt manganese oxides ($Co_xMn_{3-x}O_4$) for Fenton-like reaction in water. J. Hazard. Mater. 296, 128–137.

Ye, P., Wu, D., Wang, M., Wei, Y., Xu, A., Li, X., 2018. Coating magnetic $CuFe_2O_4$ nanoparticles with OMS-2 for enhanced degradation of organic pollutants via peroxymonosulfate activation. Appl. Sci. Res. 428, 131–139.

Yu, X., Xue, J., Yao, H., Wu, Q., Venkatesan, A.K., Halden, R.U., Kannan, K., 2015. Occurrence and estrogenic potency of eight bisphenol analogs in sewage sludge from the US EPA targeted national sewage sludge survey. J. Hazard. Mater. 299, 733–739.

Yu, L., Zhang, G., Liu, C., Lan, H., Liu, H., Qu, J., 2018. Interface stabilization of undercoordinated iron centers on manganese oxides for nature-inspired peroxide activation. ACS Catal. 8, 1090–1096.

Yu, J., Zhang, J., Zeng, T., Wang, H., Sun, Y., Chen, L., Song, S., Shi, H., 2019. Stable incorporation of MnO_x quantum dots into N-doped hollow carbon: a synergistic peroxymonosulfate activator for enhanced removal of bisphenol A. Sep. Purif. Technol. 213, 264–275.

Yun, E.-T., Lee, J.H., Kim, J., Park, H.-D., Lee, J., 2018. Identifying the nonradical mechanism in the peroxymonosulfate activation process: singlet oxygenation versus mediated electron transfer. Environ. Sci. Technol. 52 (12), 7032–7042.

Zaharieva, I., Chernev, P., Risch, M., Klingan, K., Kohlhoff, M., Fischer, A., Dau, H., 2012. Electrosynthesis, functional, and structural characterization of a water-oxidizing manganese oxide. Energy Environ. Sci. 5 (5), 7081–7089.

Zhang, H., Huang, C.-H., 2003. Oxidative transformation of triclosan and chlorophene by manganese oxides. Environ. Sci. Technol. 37 (11), 2421–2430.

Zhang, H., Huang, C.-H., 2005. Oxidative transformation of fluoroquinolone antibacterial agents and structurally related amines by manganese oxide. Environ. Sci. Technol. 39 (12), 4474–4483.

Zhang, H., Lemley, A.T., 2006. Reaction mechanism and kinetic modeling of DEET degradation by flow-through anodic Fenton treatment (FAFT). Environ. Sci. Technol. 40 (14), 4488–4494.

Zhang, H., Chen, W.-R., Huang, C.-H., 2008. Kinetic modeling of oxidation of antibacterial agents by manganese oxide. Environ. Sci. Technol. 42 (15), 5548–5554.

Zhang, T., Zhu, H., Croué, J.-P., 2013. Production of sulfate radical from peroxymonosulfate induced by a magnetically separable $CuFe_2O_4$ spinel in water: efficiency, stability, and mechanism. Environ. Sci. Technol. 47 (6), 2784–2791.

Zhang, H., Taujale, S., Huang, J., Lee, G.-J., 2015. Effects of NOM on oxidative reactivity of manganese dioxide in binary oxide mixtures with goethite or hematite. Langmuir 31 (9), 2790–2799.

Zhang, S., Fan, Q., Gao, H., Huang, Y., Liu, X., Li, J., Xu, X., Wang, X., 2016. Formation of Fe_3O_4@ MnO_2 ball-in-ball hollow spheres as a high performance catalyst with enhanced catalytic performances. J. Mater. Chem. A 4 (4), 1414–1422.

Zhang, L., Zhao, X., Niu, C., Tang, N., Guo, H., Wen, X., Liang, C., Zeng, G., 2019. Enhanced activation of peroxymonosulfate by magnetic Co_3MnFeO_6 nanoparticles for removal of carbamazepine: efficiency, synergetic mechanism and stability. Chem. Eng. J. 362, 851–864.

Zhao, Y., Zhao, Y., Zhou, R., Mao, Y., Tang, W., Ren, H., 2016. Insights into the degradation of 2,4-dichlorophenol in aqueous solution by α-MnO_2 nanowire activated persulfate: catalytic performance and kinetic modeling. RSC Adv. 6 (42), 35441–35448.

Zhao, Q., Mao, Q., Zhou, Y., Wei, J., Liu, X., Yang, J., Luo, L., Zhang, J., Chen, H., Chen, H., Tang, L., 2017. Metal-free carbon materials-catalyzed sulfate radical-based advanced oxidation processes: a review on heterogeneous catalysts and applications. Chemosphere 189, 224–238.

Zhao, Y., Li, Q., Ren, H., Zhou, R., 2017. Activation of persulfate by magnetic $MnFe_2O_4$-bentonite for catalytic degradation of 2,4-dichlorophenol in aqueous solutions. Chem. Res. Chin. Univ. 33 (3), 415–421.

Zhao, Z., Zhao, J., Yang, C., 2017. Efficient removal of ciprofloxacin by peroxymonosulfate/Mn_3O_4-MnO_2 catalytic oxidation system. Chem. Eng. J. 327, 481–489.

Zhao, X., Niu, C., Zhang, L., Guo, H., Wen, X., Liang, C., Zeng, G., 2018. Co-Mn layered double hydroxide as an effective heterogeneous catalyst for degradation of organic dyes by activation of peroxymonosulfate. Chemosphere 204, 11–21.

Zhou, Y., Jiang, J., Gao, Y., Ma, J., Pang, S.-y., Li, J., Lu, X.-T., Yuan, L.-P., 2015. Activation of peroxymonosulfate by benzoquinone: a novel non-radical oxidation process. Environ. Sci. Technol. 49, 12491–12950.

Zhou, H., Wu, S., Zhou, Y., Yang, Y., Zhang, J., Luo, L., Duan, X., Wang, S., Wang, L., Tsang, D.C.W., 2019. Insights into the oxidation of organic contaminants by iron nanoparticles encapsulated within boron and nitrogen co-doped carbon nanoshell: catalyzed Fenton-like reaction at natural pH. Environ. Int. 128, 77–88.

Zhu, C., Zhu, F., Liu, C., Chen, N., Zhou, D., Fang, G., Gao, J., 2018a. Reductive hexachloroethane degradation by S_2O_8•– with thermal activation of persulfate under anaerobic conditions. Environ. Sci. Technol. 52, 8548–8557.

Zhu, C., Zhu, F., Liu, C., Chen, N., Zhou, D., Fang, G., Gao, J., 2018b. Reductive hexachloroethane degradation by S_2O_8•– with thermal activation of persulfate under anaerobic conditions. Environ. Sci. Technol. 52 (15), 8548–8557.

Zhu, S., Li, X., Kang, J., Duan, X., Wang, S., 2019. Persulfate activation on crystallographic manganese oxides: mechanism of singlet oxygen evolution for nonradical selective degradation of aqueous contaminants. Environ. Sci. Technol. 53 (1), 307–315.

Zou, J., Ma, J., Zhang, J., 2014. Comment on electrolytic manipulation of persulfate reactivity by iron electrodes for TCE degradation in groundwater. Environ. Sci. Technol. 48 (8), 4630–4631.